Remote Sensing of Environment 152 (2014) 493–511

Contents lists available at ScienceDirect

Remote Sensing of Environment

journal homepage: www.elsevier.com/locate/rse

Validation and scale dependencies of the triangle method for the evaporative fraction estimation over heterogeneous areas

Alberto de Tomás [a,*], Héctor Nieto [b], Radoslaw Guzinski [b], Javier Salas [c], Inge Sandholt [d], Pedro Berliner [a,e]

[a] IMDEA Water Institute, Calle Punto Net 4, 28805 Alcalá de Henares, Spain
[b] Department of Geosciences and Natural Resource Management, University of Copenhagen, Øster Volgade 10, 1350 Copenhagen, Denmark
[c] Department of Geology, Geography and the Environment, University of Alcala, Calle Colegios 2, 28801 Alcalá de Henares, Spain
[d] National Space Institute, Technical University of Denmark, Ørsteds Plads, 2800 Kgs. Lyngby, Denmark
[e] Jacob Blaustein Institutes for Desert Research, Ben-Gurion University of the Negev, Sede-Boqer Campus 84990, Israel

ARTICLE INFO

Article history:
Received 21 February 2014
Received in revised form 9 June 2014
Accepted 28 June 2014
Available online xxxx

Keywords:
Evapotranspiration
Evaporative fraction
Remote sensing
Triangle method
Surface layer scintillometer
Landsat5-TM
Envisat-AATSR/MERIS
MSG-SEVIRI

ABSTRACT

Remote sensing has proved to be a consistent tool for monitoring water fluxes at regional scales. The triangle method, in particular, estimates the evaporative fraction (EF), defined as the ratio of latent heat flux (LE) to available energy, based on the relationship between satellite observations of land surface temperature and a vegetation index. Among other methodologies, this approach has been commonly used as an approximation to estimate LE, mainly over large semi-arid areas with uniform landscape features. In this study, an interpretation of the triangular space has been applied over a heterogeneous area in central Spain, using Landsat5-TM, Envisat-AATSR/MERIS and MSG-SEVIRI images. Some aspects affecting the model performance such as spatial resolution, terrain conditions, vegetation index applied and method for deriving the triangle edges have been assessed. The derived EF estimations have been validated against ground measurements obtained with scintillometer on a winter crop field during 2010–2011. When working with large spatial windows, removing areas with different topographic characteristics (altitude and slope) improved the performance of the methods. In addition, replacing the typically used NDVI with Leaf Area Index enhances the performance of the triangle method allowing a better characterization of the wet edge. Finally, results showed a relatively good performance for the EF estimates, with an RMSE of 0.11, 0.15 and 0.23 and R^2 of 0.77, 0.41, and 0.24 for Landsat, Envisat and MSG satellites respectively, showing a scale dependency on the accuracy.

1. Introduction

1.1. Background

Evapotranspiration or latent heat flux (LE) is a key component in the energy, hydrologic, carbon, and nutrient cycles. As it is indicative of water consumption from crops in agricultural lands, its determination becomes crucial for achieving a sustainable water resource management. It is mainly driven by the available radiant energy, water availability and the transport mechanism for removing the water vapor from the surface (humidity gradient and wind speed) (Batra, Islam, Venturini, Bisht, & Jiang, 2006).

The surface energy balance is generally used to obtain LE as a residual term, by combining net radiation, soil heat flux and sensible heat flux (H) estimations. At the field scale LE can be estimated using conventional techniques (Ha, Gowda, & Howell, 2012), such as eddy covariance (EC) and Bowen ratio-energy balance (BREB); or soil water balance techniques, such as surface renewal (SR) and by weighting lysimetry. However, these techniques provide basically point measurements, failing to represent the spatial heterogeneity of land surfaces and dynamic forces distribution, especially in regions with advective climatic conditions. Indeed, the changes in atmospheric forcing, water availability in the soil, vegetation structure, and land use management cause LE to have a very high spatial and temporal variability.

In that sense, remote sensing is well known for being a powerful tool when estimating regional fluxes. Several studies varying in complexity have combined remote sensing data with ancillary data to estimate LE through residual methods (Allen, Tasumi, & Trezza, 2007; Bastiaanssen, Menenti, Feddes, & Holtslag, 1998; Kustas, Perry, Doraiswamy, & Moran, 1994; Moran, Clarke, Kustas, Weltz, Amer, 1994; Norman et al., 2003; Senay, Budde, Verdin, & Melesse, 2007). Those methods which are based on a single source modeling framework, dealing with the soil–vegetation system as a single ensemble, estimate surface resistances from radiometric surface temperatures by using the excess resistance term kB^{-1} (Kustas et al., 1989). However, according to Jiang and Islam (2001) the estimation of such term requires accurate surface

* Corresponding author. Tel.: +34 918305962.
E-mail address: alberto.detomas@imdea.org (A. de Tomás).

http://dx.doi.org/10.1016/j.rse.2014.06.028
0034-4257/

observations and is very sensitive to errors in micrometeorological variables (surface wind, temperature, vegetation height, roughness length, etc.). Moreover, several assumptions about the extrapolation of atmospheric variables and resistance terms are required (Venturini, Bisht, Islam, & Jiang, 2004). On the contrary, those methods based on a two source modeling scheme, which treat the land surface as two layers (soil and vegetation), do not necessitate the use of such excess empirical resistance, but require simultaneous temperature measurements from both the soil and vegetation, not always easily accessible, or iterative methods for estimating these two temperatures (Norman, Kustas, & Humes, 1995).

According to Jiang and Islam (2003), the uncertainty in the measurement of LE is a strong argument for developing simple remote sensing methods to estimate it at regional scale. Therefore, based on the evidence that the combination of surface temperature (T_s) and a vegetation index (VI), such as the Normalized Difference Vegetation Index (NDVI), is a diagnostic of surface environmental conditions (Goward, Waring, Dye, & Yang, 1994), triangle models began to arise. They were intended to deal with some of the topics which traditional methods usually struggled with, such as (1) the complex parameterization of aerodynamic terms (e.g. aerodynamic resistance, aerodynamic temperature); (2) the absolute accuracy of satellite surface temperature retrievals; and (3) the regional availability of meteorological measurements.

As reviewed by Carlson (2007), the triangle concept was first introduced by Price (1990). Few years later Moran, Clarke, Inoue, and Vidal (1994) developed a crop water stress index justifying the theoretical background, and later on the model was elaborated upon by Carlson, Gillies, et al. (1995), Lambin and Ehrlich (1996), Gillies, Kustas, and Humes (1997), Owen, Carlson, and Gillies (1998) and by Jiang and Islam (2001). Since then, the methodology has been applied and improved by numerous researchers (Chauhan, Miller, & Ardanuy, 2003; Jiang & Islam, 2003; Long & Singh, 2013; Margulis, Kim, & Hogue, 2005; Nishida, Nemani, Running, & Glassy, 2003; Sandholt, Rasmussen, & Andersen, 2002; Wang, Li, & Cribb, 2006; Yang & Wang, 2011). Some studies take advantage of the very frequent acquisitions of geostationary satellites by expressing T_s in the T_s/VI space as an increase over time, what it is known as thermal inertia (dT_s) (Shu, Stisen, Jensen, & Sandholt, 2011; Stisen, Sandholt, Nørgaard, Fensholt, & Jensen, 2008). In the same way, other studies use a day − night T_s difference derived with heliosynchronous satellites as an approximation of dT_s, thus reducing the pixels size, both when applied to triangle based methods (Wang et al. (2006)) and more physically based approaches (Guzinski, Anderson, Kustas, Nieto, & Sandholt, 2013). As using these differences includes more information on sensible heating than T_s alone as well as they minimize systematic errors in T_s retrieval, better estimates of daily evapotranspiration can be expected than the ones obtained from instantaneous T_s.

1.2. The triangle method

Basically, the method assumes a triangular space (Fig. 1) is formed when one graphically represents T_s against a VI, as a proxy for vegetation cover, both retrieved from remote sensing data, over a certain spatial domain. Assuming that changes in T_s are due to the evaporative cooling effect of evapotranspiration, the edges of this triangular space are interpreted as follows: the wet edge represents areas where T_s is minimum and therefore maximum evapotranspiration is taking place, whereas the dry edge represents areas where T_s is maximum for a given vegetation cover and no evapotranspiration occurs. The triangular shape is given by the larger T_s range over bare soils compared to vegetation canopies, due to their different thermal conductivity. Soils have much greater mass per unit volume than vegetation canopies – where a considerable volume is filled with air – and hence present a thermal conductivity one order of magnitude larger (Goward et al., 1994; Nieto, Sandholt, Aguado, Chuvieco, & Stisen, 2011).

Jiang and Islam (2001) proposed that such space can be used to parameterize the Priestley–Taylor (PT) parameter, ϕ (Priestley & Taylor, 1972), by assuming a physical relation between the latter and the T_s–VI space. Defined by Eq. (1)

$$LE = \phi\left[(R_n - G)\frac{\Delta}{\Delta+\gamma}\right] \quad (1)$$

where LE is the latent heat flux or evapotranspiration (W m^{-2}), R_n is the net radiation (W m^{-2}), G is the soil heat flux (W m^{-2}), Δ is the slope of the saturated vapor pressure curve [kPa K^{-1}], Υ is the psychrometric constant [kPa K^{-1}], and ϕ is a substitute for the Priestly–Taylor constant, $\alpha_{PT} = 1.26$. ϕ is limited to range from $\phi_{min} = 0$, when no evapotranspiration occurs, and $\phi_{max} = \left[\frac{\Delta+\gamma}{\Delta}\right]$ at maximum evaporative rate.

In addition, evaporative fraction (EF) is described as the ratio of available energy (R_n–G) which is used to convert liquid water into water vapor (Eq. (2)):

$$EF = \frac{LE}{R_n - G} \quad (2)$$

which in combination with Eq. (1) can be expressed as:

$$EF = \phi\left[\frac{\Delta}{\Delta+\gamma}\right]. \quad (3)$$

Thus, following the previous approach, the wet edge corresponds to areas where the PT parameter and EF are at maximum (ϕ_{max}, EF = 1), whereas the dry edge corresponds to areas where the PT parameter and EF are null (ϕ_{min}, EF = 0). All the pixels in between have intermediate ϕ and EF values (Fig. 1). When both edges are estimated, EF can be computed for all cloud-free pixels based on their relative position between the edges via interpolation. Facing the impossibility of determining the true dry edge from remote sensing observations (Stisen et al., 2008), such interpolation must be completed in two steps: firstly obtaining ϕ_{min} for each NDVI interval, and secondly obtaining ϕ_i within each NDVI interval. Otherwise, working with the true dry edge would involve an inversion of a model for estimating ET (Moran, Clarke, Inoue, et al., 1994). Afterward, evapotranspiration rates can be calculated by combining EF with an estimate of the available energy (R_n–G).

As pointed out by Jiang and Islam (2001), the use of contextual information for deriving ϕ allows the application of Eq. (1) over large heterogeneous areas in contrast with α_{PT}, which is merely applicable for wet surface equilibrium conditions. ϕ represents an effective surface resistance to evapotranspiration since it is a replacement for the aerodynamic term of the Montetih's equation (Montetih, 1965), from which it is developed. Yet, as it is not related to a single surface attribute,

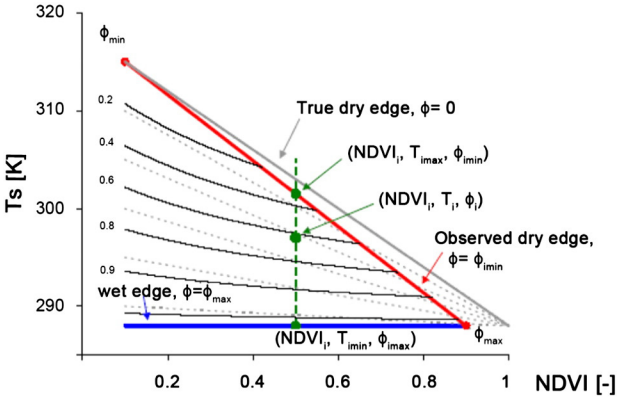

Fig. 1. Conceptual triangular space.
Adapted from Stisen et al. (2008).

it takes no account of the aerodynamic properties and physiological behavior of the surface, and this can lead to major uncertainties during extreme conditions (wind, humidity) (Stisen et al., 2008). Therefore, the methodology involves an assumption of uniform coupling with the atmosphere and surface roughness (e.g., incoming radiation, air temperature, wind speed, and canopy structure) over the area of interest (Jiang & Islam, 1999, 2001, 2003; Long, Singh, & Scanlon, 2012).

For a proper model performance both areas with large evaporation and low T_s as well as those with no evaporation and high T_s, must be recognizable within the boundaries of the domain used to derive the triangle. Assuming that those different situations are not due to changes in atmospheric forcing conditions or surface roughness but due to variations in water availability, a heterogeneous study area large enough to guarantee certain number of pixels with a wide range of soil moisture conditions and vegetation cover, is required. So, the coarser the spatial resolution of the input data, the bigger the domain size required, since a larger area is needed for the definition of the triangle. However, ensuring uniform atmospheric conditions requires relatively small areas, and this might compromise the previous need.

Furthermore, clouds, sloping terrain, shading and standing water cause variations in T_s retrievals and might be the source of errors when establishing the triangle wet edge (Long & Singh, 2012; Tang, Li, & Tang, 2010). As it is assumed that changes in T_s are mainly due to the evaporative cooling effect, rather than elevation variation, all the pixels within the spatial domain should have a similar elevation. According to the preceding requirements, it becomes reasonable to create a mask in order to apply the triangle over non-water bodies, cloudless surfaces with similar characteristics, such as altitude, slope and vegetation physiology (Carlson, 2007; Carlson, Capehart, et al., 1995).

Finally, NDVI has been widely used as the proxy for the vegetation cover in the triangle due to its simplicity. However, according to the relation displayed in Fig. 2a from Han, Wang, Yang, Liu, and Wang (2006), when NDVI is close to saturation (~1) LAI, and hence vegetation cover, is still increasing (from 6 to 10), as it includes green contributors like understory under upper canopies. Using LAI instead of NDVI should avoid the triangular space being cut into a trapezoid shape due to limiting NDVI, as shown in Fig. 2b.

1.3. Objectives

This research aims at assessing the triangle approach over a heterogeneous area for estimating daytime averages of EF. We will focus on studying how the method performance depends on spatial resolution, terrain conditions (vegetation classes, altitude, slope), type of VI, and edge algorithms used. For that purpose the triangle method is applied over a series of different satellite imagery dataset at different spatial resolutions, including MSG-SEVIRI, Envisat-AATSR/MERIS and Landsat5-TM, to obtain EF estimations and to compare them with ground scintillometer measurements. The method is tested with and without masking terrain conditions, as well as using either NDVI or LAI as VI in the triangle, and different configurations of the dry and wet edge algorithms. Furthermore, no previous works of comparable validation of EF estimations were found in our study area. Despite of the potential of SEVIRI for estimating the thermal inertia, this concept remains out of the scope in this paper in order to compare results between datasets. A description of the methodology is presented in Section 2. Section 3 presents the annual variation of some physical parameters and the triangle performance, which is discussed in Section 4. Finally, Section 5 contains a summary of the main results obtained, including advantages and disadvantages of different parameters and algorithms, and the general conclusions from this research.

2. Methodology

2.1. Study area and field measurements

This study was conducted on the Henares River basin (Fig. 3a), which belongs to the Tagus River hydrographic basin, in central Spain. With a total surface area of 4136 km^2, the basin's highest reliefs (above 1500 m) are located to the northwest while the rest, mainly corresponding to alluvial plains and a wide system of river terraces, is relatively flat (~550 m). A north–south gradient characterizes the mean annual precipitation, ranging from 700 mm to 400 mm, with rainfall events being more frequent during spring and autumn, as it is typical in continental Mediterranean climates. The land cover follows both the elevation and rainfall distribution. Thus, deciduous and evergreen forests together with scrub and pasturelands are quite abundant in the mountainous areas, whereas crops dominate flatter territories (Fig. 3b): maize as irrigated summer crop and oats, wheat or forage crops as non-irrigated winter crops. Within the basin there are three main population centers (more than 80,000 inh) demanding water from the river: Guadalajara, Torrejón de Ardoz and Alcalá de Henares.

Close to Alcalá de Henares, at an altitude of 615 m there is a 20 ha experimental field, La Canaleja (40° 30′ N, 3° 18′W), where ground measurements were taken over two different growing seasons and crop types: wheat (April 2010–July 2010) and oats (October 2010–Jun 2011). Surrounded by urban areas, as well as different types of crops, scrubs, and fallow lands, the landscape of the study site is particularly

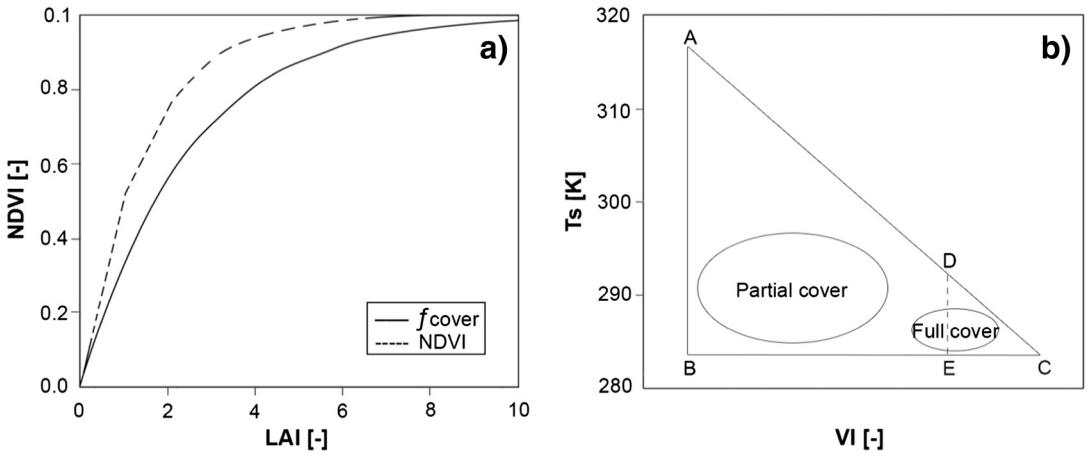

Fig. 2. a–b. a) NDVI–LAI relationship; b) LAI triangular shape (ABC) vs. NDVI trapezoid (ABDE). Adapted from Han et al. (2006).

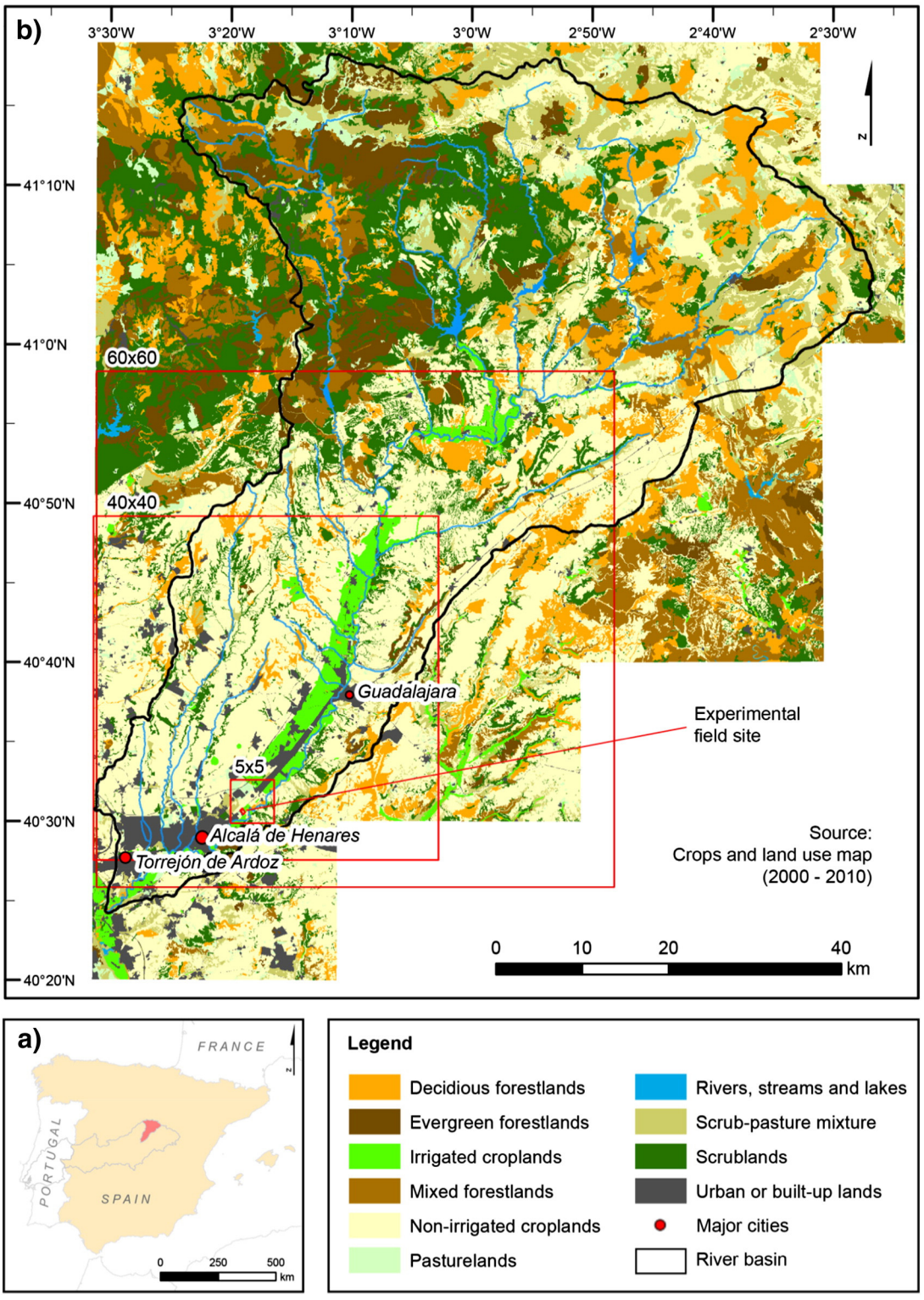

Fig. 3. a–b. Study area: a) Henares River basin location; b) Land cover map and domain window sizes: 5 × 5 km for Landsat, 40 × 40 km for Envisat, and 60 × 60 km for SEVIRI. (For a better interpretation of the colors in this figure, the reader is referred to the web version of this article.)

heterogeneous (Fig. 3b). At this point, the river flows eroding the steep slopes of the Paramo of La Alcarria (Gutiérrez-Elorza et al., 2002) that dominates the left bank, with a mean altitude around 200 m higher than the right bank.

A surface layer scintillometer was used for measuring sensible heat flux (H). This technology is based on the principle of measuring the intensity variations of an electromagnetic beam between a transmitter and an emitter, in our case along a 100 m path and at 1.75 m height over the crop. The instrument is able to derive sensible heat flux by relating the structure function parameter of temperature (C^2_T) to the structure parameter for the refractive index (C^2_n), which can be directly measured by the scintillometer. The reader is referred to Hill (1992) for a detailed review regarding scintillometry. Likewise, a meteorological station equipped with psychrometers, a net radiometer and a soil heat

flux plate recorded the available net energy (R_n–G) necessary for obtaining the latent heat flux as a residual term of the energy balance (Eq. (4)):

$$LE = R_n - G - H. \quad (4)$$

All fluxes were measured with a 15 min frequency. EF is frequently assumed to remain constant during the daytime, and this can be used in order to calculate daily evapotranspiration (Anderson, Norman, Diak, Kustas, & Mecikalski, 1997; Bastiaanssen, Thiruvengadachari, Sakthivadivel, & Molden, 1999; Crago, 1996b; Crago & Brutsaert, 1996). Therefore daytime averages of EF based on that interval (in particular 08:00–12:00 UTC) were calculated after applying Eqs. (4) and (2). As a consequence of using the residual method, LE, and therefore EF, accumulates errors from the other flux components which can be either additive or compensating. Despite these uncertainties and those related to scale dependencies, these datasets were assumed reliable and hence were used for validation.

2.2. Satellite data

Several satellite platforms with different spatial and temporal resolutions were used in this study. From coarser to finer spatial resolution, as detailed in Table 1: MSG-SEVIRI, Envisat-AATSR/MERIS and Landsat5-TM.

Landsat5-TM imagery (path 201/row 32) was acquired from the United States Geological Survey (USGS — http://glovis.usgs.gov/, last accessed 10th February 2014). Bands in the visible and near-infrared parts of the spectrum (bands 1–5 and 7) are acquired at 30 m spatial resolution, while the thermal band (6) is acquired at 120 m and resampled to 30 m using cubic convolution, according to the standard processing at USGS (http://landsat.usgs.gov/Landsat_Processing_Details.php, last accessed 10th February 2014). These data are preprocessed to a 1 T level standard terrain correction, providing systematic radiometric and geometric accuracy — enabling pixels in the image to correspond to real world coordinates (WGS84 UTM 30 N projection) by incorporating ground control points while employing a Digital Elevation Model (DEM) for topographic accuracy. Due to Landsat's heliosynchronous orbit the overpass repeat cycle is 16 days, limiting its usefulness for duties such as operational monitoring of water fluxes — despite its high spatial resolution.

The European Space Agency's (ESA) Envisat satellite, no longer operational, completed a global coverage within 2–3 days. The Advanced Along-Track Scanning Radiometer (AATSR) sensor onboard was equipped with a dual-view system which allowed two near simultaneous observations of the same area, one at near-nadir with 1 km resolution and one forward looking at a viewing angle of ~55° with a resolution of around 2 km. It was equipped with 2 thermal bands for the estimation of the land surface temperature by a split-window algorithm. The radiances at the top of the atmosphere (ATS_TOA_1) product was collected from the on-line MERCI system (http://ats-merci-uk.eo.esa.int:8080/merci, last accessed 10th February 2014). On the other hand, the Medium Resolution Imaging Spectrometer (MERIS) sensor, also onboard Envisat, operated only in the solar spectrum with 15 bands. Although MERIS original spatial resolution was 300 m, we downloaded the Reduced Resolution level 2p product (MER_RR_2p), also from the MERCI system, in order to use it in conjunction with AATSR data at 1 km. MER_RR_2p provided, among other data, atmospherically corrected surface reflectances in 14 spectral bands. Both datasets, AATSR and MERIS were then reprojected to WGS84 UTM 30 N, and subset to the same spatial extent in order to be combined in further analyses. The resampling was performed using nearest neighbor interpolation.

Finally, the Spinning Enhanced Visible and InfraRed Imager (SEVIRI) sensor onboard the geostationary Meteosat Second Generation satellites (MSG) provides very high frequent acquisitions (15 min) of both optical and thermal infrared data. However, that compromises the spatial resolution (~3.1 km spatial sampling at nadir) as well as angular effects due to the observation geometry inherent of a geostationary satellite (Fensholt, Sandholt, Stisen, & Tucker, 2006; Rasmussen, Pinheiro, Proud, & Sandholt, 2010). Similarly to AATSR, 2 split-window thermal bands are available, in addition to another 10 different wavelengths bands. Leaf Area Index (LAI) and Land Surface Temperature (LST) products from the Land Surface Analysis Satellite Applications Facility (LSA SAF — http://landsaf.meteo.pt/, last accessed 10th February 2014) were used in this research. The images, corresponding to the European region, were resampled from the original ~3.5 km geostationary projection to 4 km WGS84 UTM 30 N by a nearest neighborhood resampling method. Such pixel size was selected for being a multiple of 1 km and therefore convenient for the observation geometry of SEVIRI over our study area.

Table 1
Comparison of satellite resolutions.

Platform/sensor	Spatial resolution (thermal/optical)	Vegetation index used	Thermal bands used	Revisit time
Landsat5 -TM	120/30 m	NDVI	11.45 μm	16 days
Envisat AATSR/MERIS	1 km/300 m	NDVI/LAI	10.8 μm 12 μm	2–3 days
MSG SEVIRI	~4 km	LAI	10.8 μm 12 μm	15 min

2.3. Methodology

The following paragraphs describe the methodology (Fig. 4) applied in this study, from processing of the satellite data and the retrieval of the algorithm inputs (T_s and VI) to the final estimation of EF, including the development of a terrain mask.

2.3.1. Satellite imagery processing

2.3.1.1. Landsat processing. Landsat optical bands were atmospherically corrected prior to being used. Due to the low radiometric resolution of the TM sensor (8 bits), the simple dark object subtraction technique from Chavez (1996) was applied. Once the surface reflectance was obtained, the NDVI was calculated according to the original formula from Rouse, Harrs, Schell, Deering, and Harlan (1974):

$$NDVI = \frac{\rho_{NIR} - \rho_R}{\rho_{NIR} + \rho_R} \quad (5)$$

where ρ_{NIR} and ρ_R are the reflectances in the near-infrared and red regions of the spectrum.

Then, brightness temperature was computed from the at-sensor radiance of the thermal band, following the equations from Chander, Markham, and Helder (2009). Using one channel brightness temperature as a surrogate of T_s may be affected by surface emissivity and water vapor absorption effects. However, as found out by Venturini et al. (2004), absolute values of temperature do not dramatically change the relationship between NDVI and T_s during clear sky days. Since the triangle method assumes homogeneous atmospheric forcing within the modeling domain, a constant precipitable water vapor is assumed to be present as well, given that spatial variation in precipitable water vapor would modify the incoming radiation at the surface. In the case of the Landsat spatial domain (5 × 5 km) we therefore assume that the precipitable water vapor remains constant and hence the atmospheric correction of the brightness temperatures will be the same for the whole spatial domain. Furthermore, the triangle method is based on the relative position within the triangular space and thus, no accurate T_s estimations are required. In order to work only with cloud free pixels in the area, a cloud mask based on simple thresholds of NDVI (<0.1) and the brightness temperature (<280 K) was created.

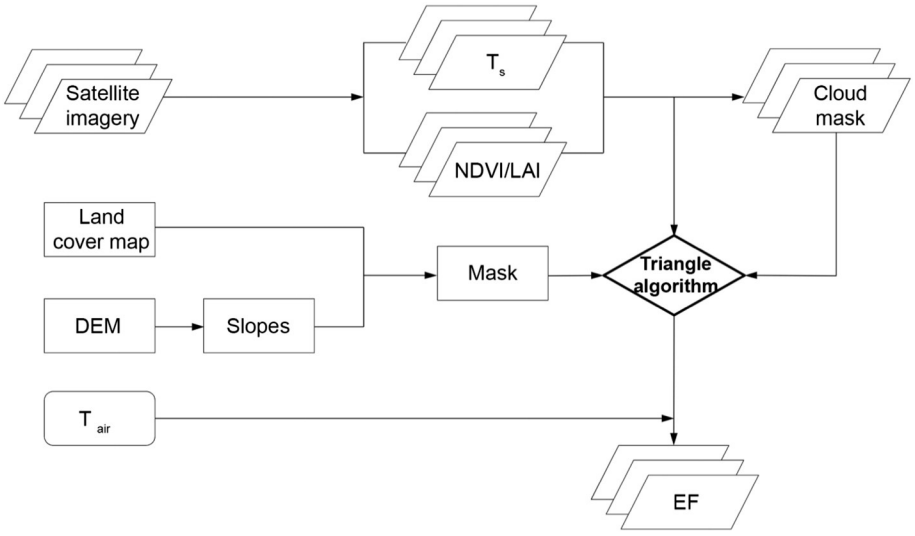

Fig. 4. Methodology scheme.

The performance of the cloud mask was visually checked in all the scenes selected in this study showing a good consistency.

2.3.1.2. Envisat processing. T_s was retrieved from AATSR data using the Sòria and Sobrino (2007) split-window algorithm for the near-nadir brightness temperatures. Following the modified APOLLO algorithm (Plummer, 2008), a cloud mask was created for every image. Besides the brightness temperatures, precipitable water vapor and directional emissivity are required in the split-window algorithm. The split-window variance–covariance ratio algorithm proposed by Li, Jia, Su, Wan, and Zhang (2003) was used in order to retrieve the precipitable water vapor, whereas the directional emissivity was estimated from Leaf Area Index (LAI) and using the radiative transfer model 4SAIL (Sobrino, Jiménez-Muñoz, & Verhoef, 2005; Verhoef, Jia, Qing, & Su, 2007) with emissivity values for soil and vegetation of 0.95 and 0.98 respectively. LAI was derived from MERIS MER_RR_2p reflectances by using the algorithm developed by Baret et al. (2006), which is implemented as a module in the ESA's BEAM open-source toolbox (http://www.brockmann-consult.de/cms/web/beam/, last accessed 10th February 2014).

2.3.1.3. SEVIRI processing. As detailed in the LSA SAF products description (http://landsaf.meteo.pt/products/prods.jsp, last accessed 10th February 2014), the retrieval of MSG-SEVIRI TS is based on the generalized split-window algorithm by Wan and Dozier (1996), which requires land surface emissivity (ε) as input. In the same way, the retrieval of ε is based on the Vegetation Cover Method (VCM) from Caselles, Valor, Coll, and Rubio (1997) that relies on the use of a geometrical model to compute an effective emissivity based on the knowledge of the Fractional Vegetation Cover (FVC), also computed by the LSA SAF. Moreover, a cloud mask is generated by the Nowcasting and Very Short Range Forecasting Satellite Application Facility (NWC SAF) software. Thus, the cloud-free FVC product, corrected from view/sun angles and anisotropy effects, is used to directly obtain the LAI product, which ranges from 0 to 10. In order to do so, the LSA SAF service implemented an algorithm which is a backup solution of the physical-model inversion method by Garcia-Haro, Fernando Camacho-de, and Melia (2006). The algorithm employs a semi-empirical exponential relationship with the FVC product, as in Roujean and Lacaze (2002), assuming spherical orientation of the foliage and a coefficient which is function of the leaf albedo (fitted to a random distribution of the vegetation).

2.3.2. Terrain mask

A digital elevation model (horizontal resolution of 25 m) from the Spanish National Geographic Institute (http://www.ign.es/ign/layoutIn/modeloDigitalTerreno.do, last accessed 10th February 2014), was used to remove areas with heights differing more than 500 m from the experimental site altitude as well as terrain with slopes steeper than 15°. Likewise, urban areas, major water bodies and woodland land cover types were also excluded based on the Crops and Land Use Map (*MCA — Mapa de Cultivos y Aprovechamientos*) 2000–2010 (scale 1:50,000) of the Ministry for Agriculture, Food and the Environment (http://www.magrama.gob.es/es/cartografia-y-sig/publicaciones/agricultura/mac_2000_2009.aspx, last accessed 10th February 2014), leaving only those land surfaces with similar roughness e.g. crops, scrubs, pastures and mixtures of all of them.

2.3.3. Dry and wet edge algorithms

Different algorithms for establishing the wet and dry edge of the triangle were tested, as described next. In order to better compare results by setting the same configuration in all cases, the ϕ value was constrained by using $1/\left[\frac{\Delta}{\Delta+\gamma}\right]$ as ϕ_{max}, and ϕ_{min} was calculated by the non-linear interpolation proposed by Stisen et al. (2008) as part of the two-step interpolation. The latter is justified by assuming that the true dry edge cannot be determined when working with either NDVI or LAI.

2.3.3.1. Dry edge.

- The *Simple* dry edge algorithm was mainly used, whose steps are described as follows:
  i. The algorithm splits the T_s pixels into a number of bins based on the VI value of a corresponding NDVI/LAI pixel. The VI step size of the bins was set in all cases to 0.01 for Landsat and Envisat and 0.05 for SEVIRI, and the value of minimum VI bin to 0.1.
  ii. For each bin it finds the maximum and minimum T_s values, the latter one for calculation of the wet edge.
  iii. It removes all the maximum T_s values which are to the left in the triangle graph (with corresponding lower VI value) of the maximum T_s of the image as well as those maximum T_s lower than the mean minimum T_s of the image.
  iv. Finally, it performs a linear fit through the remaining T_s max values and the corresponding VI bin values and uses the fit as the dry edge.
- The *Tang* dry edge algorithm also divides the T_s pixels into a number of bins based on the VI values although the way in which the

maximum value of each bin is calculated and the way in which the outliers are removed is more complicated. For further details see Tang et al. (2010). The implementation of the *Tang* algorithm in our routines was slightly modified compared to the original, since the maximum T_s values which are to the left (in the triangle graph) of the maximum T_s of the image, are also removed.

2.3.3.2. Wet edge.

- *Variable max VI* algorithm, where T_s min is the value of the dry edge either at a given value of NDVI/LAI (set to 0.9 and 1.9, respectively) or at the actual maximum value of NDVI/LAI found in the image, whichever is smaller.
- *Mean* algorithm, where the T_s min is equal to the mean of the minimum T_s values from a number of bins (set to 10) with the largest VI values.

2.3.4. Obtaining EF

From the meteorological station records of air temperature (T_a), $\left[\frac{\Delta}{\Delta+\gamma}\right]$ parameter was calculated and assumed to be constant for the rest of the spatial domain. Previous works have shown that although dependent on T_a, the sensitivity of the $\left[\frac{\Delta}{\Delta+\gamma}\right]$ parameter to the variation of temperature is very small (Tang et al., 2010; Venturini et al., 2004). In operational applications, T_a can be obtained either by a linear regression between T_s and T_s–T_a, by using the minimum surface temperature, the average temperature of water bodies, or semi-empirical methods based as well on the T_s/NDVI relationship (Nieto et al., 2011).

Finally, combining the estimated ϕ from the triangle algorithm with the measured $\left[\frac{\Delta}{\Delta+\gamma}\right]$ parameter, the instantaneous EF was obtained.

2.3.5. Triangle performance analyses

The described methodology was applied to evaluate the triangle performance in the following cases:

- Inter-dataset model comparison with the terrain mask incorporated: the same dry and wet edge algorithms were applied to T_s/VI data obtained with the three different sensors in order to be able to compare differences of performance related to the spatial resolution and window domain size.
- Effects of masking terrain conditions: the same configuration was tested without masking terrain conditions (land cover, altitude and slopes), to evaluate the influence of the mask on the method performance.
- Effects of the vegetation index choice: in order to evaluate how the type of VI used influences the results, triangles using either Envisat-MERIS NDVI or LAI products were tested.
- Best dry/wet edge algorithm: different combinations of both dry and wet algorithms were tested in order to obtain the best possible results.

To analyze and compare results, the statistical measures shown in Table 2 were calculated in every section.

Table 2
Statistical measures. Note: P_i is predicted, O_i is observed and n is the number of samples.

Statistical measure	
Root mean square error	$\mathrm{RMSE} = \sqrt{\frac{1}{n}\sum_{i=1}^{n}(P_i - O_i)^2}$
Bias	$\mathrm{Bias} = \overline{P_i} - \overline{O_i}$
Mean absolute error	$\mathrm{MAE} = \frac{1}{n}\sum_{i=1}^{n}\lvert P_i - O_i\rvert$
Coefficient of determination	$R^2 = \left\{ \frac{\sum_{i=1}^{n}\left(O_i-\overline{O}\right)\left(P_i-\overline{P}\right)}{\left[\sum_{i=1}^{n}\left(O_i-\overline{O}\right)^2\right]^{0.5}\left[\sum_{i=1}^{n}\left(P_i-\overline{P}\right)^2\right]^{0.5}} \right\}^2$

3. Results

3.1. Annual variation of physical parameters

Fig. 5 represents the annual variation of some physical parameters related to EF, observed at the experimental site during the two campaigns. Between November 2010 and January 2011 there are missing values for both ϕ and EF, due to technical problems with the instrumentation. Rainfall events (Fig. 5a) during the springtime in 2011 are more frequent and abundant than those for the same period in 2010, conditioning the rest of parameters described next.

Fig. 5b displays LAI variation for wheat (first campaign) and oats (second campaign), retrieved from Envisat-MERIS. The growing season starts in March and reaches its maximum around middle of May, when the crop senescence begins, being harvested by the end of June. LAI maximum values for the oats are slightly higher than those for the wheat (1.8 and 1.6 respectively). LAI residual values for the bare soil period range between 0 and 0.5. It must be noticed that LAI values oscillate on consecutive dates, most likely due to imperfect atmospheric corrections, angular effects and uncertainty related to the LAI model inversion.

Seasonality of field site T_s can be observed in Fig. 5c, where temperature gradually increases from 10 to 30 °C along the growing season. The highest values for ϕ (Fig. 5d) in that period correspond to the highest EF observed values (Fig. 5e). They decrease concurrently as well, thus showing the small influence of changes of air temperature in Eq. (3). During the time when there is still bare soil a maximum of ~0.5 ϕ value should be expected in dry conditions. However, since ϕ is highly influenced by rainfall, it might reach values close to 1 or above. The same is observed for the EF values, which vary from 0.3 to 0.8 during the same period. Theoretically, ϕ_{max} is meant to be 1.26 (Priestley & Taylor, 1972), but it can be seen that this value can be exceeded after a rainfall, especially during the second growing season. EF daily standard deviation results for the intervals 08:00–12:00 UTC remain close to zero for the two growing periods. Only after heavy or long-lasting rain events or cloudy days, the EF daytime variability increases.

3.2. Triangle performance

In the following sections, several comparisons of instantaneous (acquisition time 10:45 UTC for all sensors) EF estimations from remotely sensed data with daytime averages of EF observations from field measurements are analyzed. While for Envisat and SEVIRI the corresponding pixel containing the experimental field was selected for this purpose, an average of the pixels contained within the experimental field is used for Landsat. Prior to comparison, inconsistent values (i.e. EF negative or higher than 1), occurring when pixels are outside the boundaries of the triangle edges, were removed. Rainfall events increase moisture content, and might lead to EF values higher than 1. The difference of the number of valid cases for each satellite is a consequence not only of the former but also of the temporal resolution.

3.2.1. Domain size selection

In order to obtain better results, an optimal window size was determined for each dataset by testing several domain sizes over the study area, increasing from an initial small one, until a reasonable triangular shape could be formed. As a result, a 5 × 5 km window size was selected for Landsat (27,889 pixels), 40 × 40 km for Envisat (1540 pixels) and 60 × 60 km for SEVIRI (204 pixels), as shown in Fig. 3b.

Fig. 6 shows Landsat domain dependencies present when comparing 5 × 5 km to 60 × 60 km window domain sizes for three selected dates with minimum, medium and maximum EF rates, and therefore soil moisture conditions (20100623, 20100404 and 20110407, respectively). As the domain gets larger, the dry edge becomes warmer and

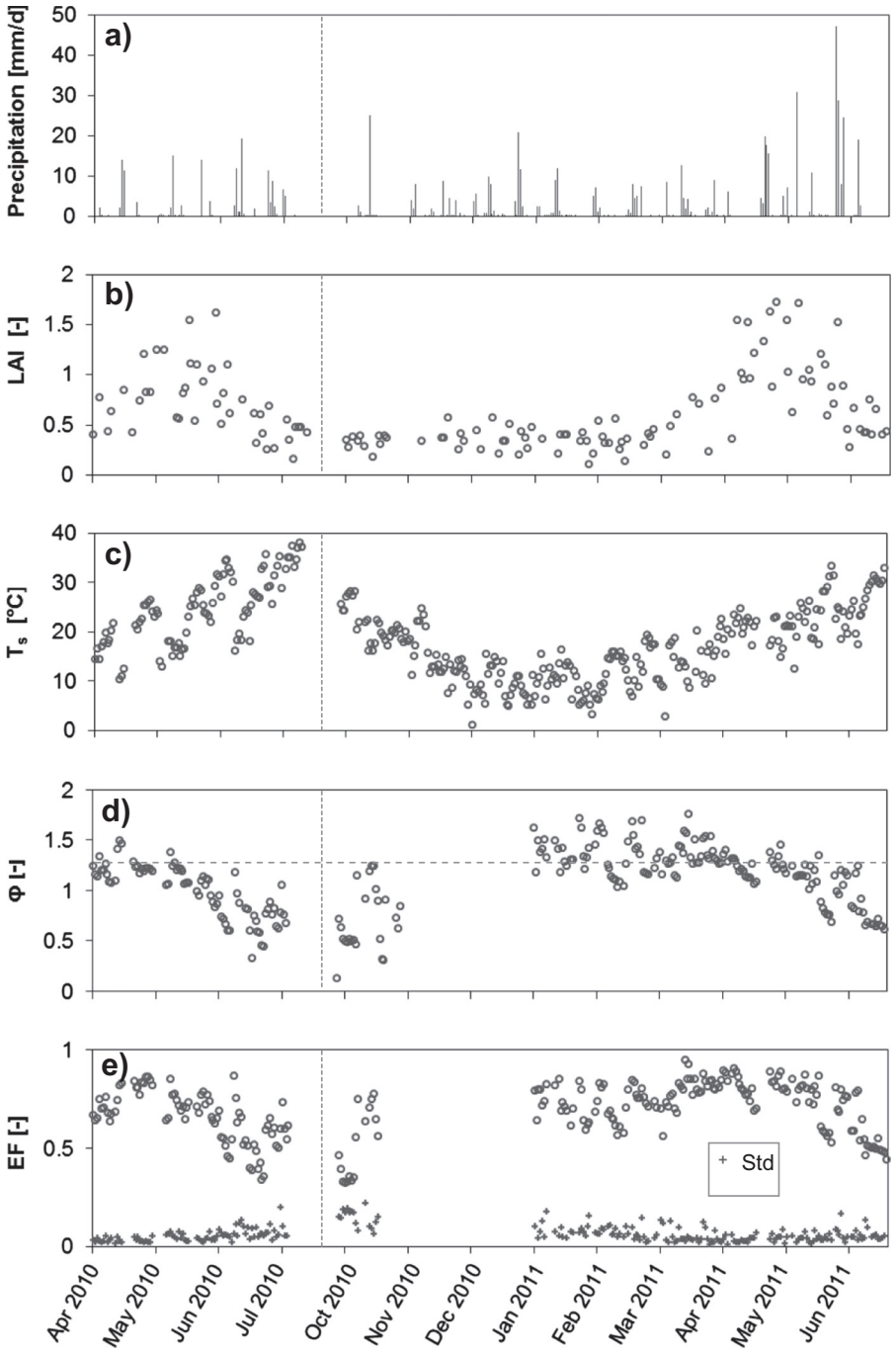

Fig. 5. Annual variation at the study site of: a) daily precipitation; b) LAI retrievals from Envisat-MERIS; c–e) 08:00–12:00 UTC interval daily averages of in situ $T_{s,}$ estimated from the longwave radiometers deployed in the field, as well as ϕ and EF with its standard deviation (Std.). The horizontal dashed line in d) represents the typical value of α_{PT}–1.26. The vertical dashed line represents a time break between field campaigns.

moves upward. The wet edge established by the *Simple Variable max VI* (*S. Var max VI*) algorithms moves upward too, while the wet edge established by the *Simple Mean* (*S. Mean*) algorithms becomes colder moving toward the opposite direction. Table 3 lists the estimated EF for both domains and algorithms' configuration for the wet edge. EF results for the 5 × 5 km domain size and *S. Var max VI* algorithm are the most similar to the observed EF measurements. Enlarging the domain size when using this algorithm worsens results as seen for the 60 × 60 km domain size estimations. Results for both domain sizes and *S. Mean* algorithm present worse estimations and remain quite similar, except for the driest situation where there is a noticeable change.

3.2.2. Dataset model comparison

In order to better compare the performance of each platform, we applied the same method for the retrieval of the triangle edges for each of the three datasets. The *Simple* and the *Variable max VI* algorithms' combination showed better outcomes in preliminary results (partially shown in the previous analysis) and therefore it was used with all images. However, it has to be considered that NDVI remained as the vegetation index for Landsat, whereas LAI was used for Envisat and SEVIRI.

Fig. 7 compares EF estimations to field measurements and Table 4 lists the statistics for each sensor. In general, estimations are good,

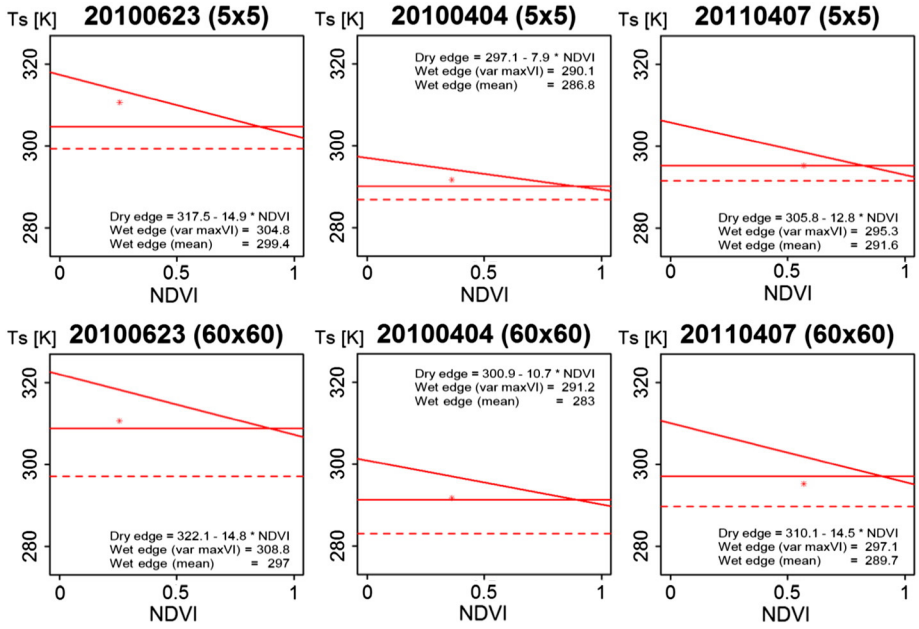

Fig. 6. Landsat domain dependencies on the establishment of the triangle edges, using *Simple* algorithm for the dry edge and *Var max VI* (solid line) or *Mean* (dashed line) algorithms for the wet edge. The relative position of the experimental field site with respect to the edges is represented by an asterisk.

although the performance is closely related to the spatial resolution. Hence, RMSE ranges from 0.11 for Landsat and 0.15 for Envisat to 0.23 for SEVIRI and consequently similar pattern is observed for the MAE (0.09, 0.11 and 0.19, respectively). Furthermore, R^2 decreases as the resolution decreases (0.77, 0.41 and 0.24 respectively), but that is also depending on the number of available acquisitions and hence related to the temporal resolution of each sensor. While Landsat and Envisat relations remain relatively unbiased, SEVIRI estimations are slightly overestimated. The Analysis of Variance (ANOVA) p-values confirm a statistically significant relationship between observations and estimations at the 99% confidence level.

In order to assess whether the worse results when using SEVIRI and Envisat data are just due to the scale mismatch present during the validation or due to the different triangle spatial domain extents between sensors, Landsat derived EF from the previous analysis (using the *Simple* and *Variable max VI* algorithms) were resampled to match Envisat (1 km) and SEVIRI (4 km) pixel sizes by averaging all the 30 m pixels within each coarse resolution pixel (1 km and 4 km). Table 5 lists the statistic discrepancies between these resampled Landsat results and the observed measurements. As the size of the resampled resolution increases, statistics worsen and become consistent with the corresponding sensor statistics showed in Table 4. Thus, RMSE and MAE are 0.12 and 0.09 respectively for the 1 km aggregation (RMSE = 0.15 and MAE = 0.11 with Envisat), and 0.25 and 0.21 respectively for the 4 km aggregation (RMSE = 0.23 and MAE = 0.19 for SEVIRI). Despite R^2 values being slightly better (0.57 and 0.33) than those showed in Table 4, ANOVA p-values are worse, even showing no statistically significant relation with observed measurements for the 4 km aggregation, due to the lower number of Landsat scenes compared to Envisat and SEVIRI.

Table 3
Experimental field site T_s, NDVI and EF observations, compared to Landsat EF estimations for both domain sizes and algorithms' configuration.

Date	Experimental field			EF_{est} 5 × 5		EF_{est} 60 × 60	
	T_s	NDVI	EF_{obs}	*S. Var max VI*	*S. Mean*	*S. Var max VI*	*S. Mean*
20100623	310.7	0.26	0.34	0.36	0.24	0.81	0.38
20100404	291.7	0.36	0.75	0.65	0.41	0.93	0.45
20110407	295.2	0.57	0.91	1	0.66	1.25	0.70

3.2.3. Mask effect

Fig. 8 and Table 6 show the effect in the EF estimates when the mask based on topography and vegetation type is removed. We used the same dry and wet algorithms' configuration as in the previous section.

Both Landsat and Envisat RMSE, MAE and R^2 (0.10, 0.09, 0.80 and 0.15, 0.12, 0.46, respectively) are very similar to the previous masked results. Thus, ANOVA p-values still confirm a statistically significant relationship between those observations and estimations at the 99% confidence level. However, SEVIRI statistics get worse in this case. RMSE, MAE and R^2 decreased to 0.36, 0.26 and 0.06, respectively. Accordingly, ANOVA statistics show no relationship between observations and estimations.

3.2.4. Vegetation index comparison

In order to compare the performance of each vegetation index used, Envisat NDVI and LAI products derived on the same dates were tested with both the *S. Mean* and *S. Var max VI* algorithms for the dry and wet edge determination and compared to field measurements, as shown in Fig. 9. Analysis statistics are listed in Table 7. Despite the general triangle performance being good with Envisat data in both cases, some differences can be found when using either LAI or NDVI.

In general, better results are obtained when using LAI as the vegetation index. For the *Mean* wet edge algorithm it can be observed that LAI results are better than those from using NDVI. RMSE is 0.14 compared to 0.16, MAE is 0.11 compared to 0.14 and R^2 is 0.62 for LAI and 0.38 for NDVI. The same relation can be found in the *Var max VI* algorithm results. RMSE and MAE are higher for NDVI than for LAI (0.19 and 0.14 compared to 0.14 and 0.10, respectively). All cases present a statistically significant relationship at 95% confidence level between the observed and the estimated values.

3.2.5. Dry edge algorithm comparison

This last section analyzes the improvement obtained when using the *Tang* algorithm for establishing the dry edge on Landsat imagery. Fig. 10 compares EF estimations to field measurements and Table 8 lists the statistics analyses. RMSE, MAE and R^2 (0.07, 0.05 and 0.90, respectively)

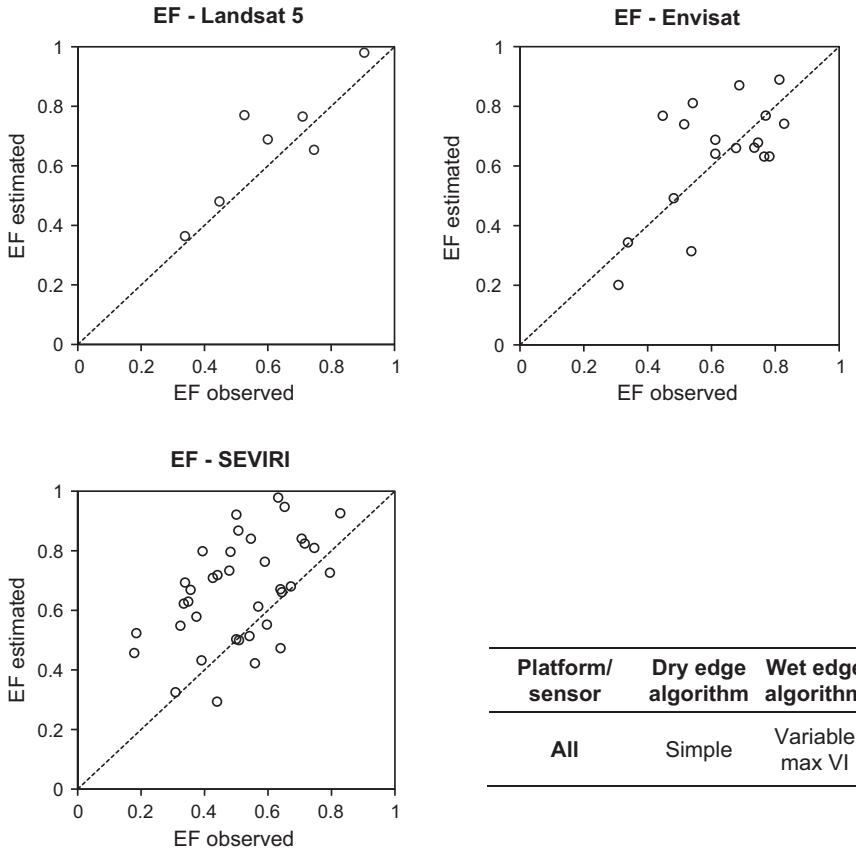

Platform/ sensor	Dry edge algorithm	Wet edge algorithm
All	Simple	Variable max VI

Fig. 7. Comparison of remotely sensed EF estimates, using the same algorithms for each dataset, against EF field measurements.

show better results than the ones obtained with the *Simple* dry edge (Section 3.2.2). In the same way, ANOVA p-value confirms a statistically significant better relationship between observations and estimations at the 99% confidence level.

4. Discussion

Different approaches of the triangle method have been developed (Shu et al., 2011; Stisen et al., 2008; Tang et al., 2010; Wang et al., 2006; Yang & Wang, 2011) showing comparable accuracy with our results. More recently, Long and Singh (2012) presented a trapezoid model capable of discriminating vegetation transpiration from soil surface evaporation based on a two-source scheme and Merlin (2013) proposed an original interpretation of the wet edge of the T_s–albedo space. It must be considered that some uncertainty is assumed due to the large scale difference between ground measurements and the satellite pixel size, besides uncertainty on account of using the residual method for obtaining LE from in-situ measurements or LAI products. Nevertheless, our results indicate moderately good agreement with ground measurements, with errors around 10% of EF for the case of Landsat. Our goal was not only to discuss the model performance itself but also, more importantly, to study how results might be influenced by some of the aspects which are discussed next.

Rainfall determines soil moisture availability and hence it is considered to be the main limiting factor for vegetation growth in Mediterranean climates (French & Schultz, 1984). ϕ, which in turn depends on soil moisture, regulates EF as expressed in Eq. (3). That relation can be observed in Fig. 5, where the copious precipitation during the second campaign (April–June 2011) produced higher ϕ, EF and therefore higher LAI values, meaning higher crop yield rates. Rainfall during this period has a more direct effect on crop growth, as it corresponds to their maximum growing rate stage. In the same way, when is there still bare soil, an excess of soil moisture due to rainfall can produce ϕ values higher than the expected α_{PT}. And so, throughout the rest of the period EF remains relatively high, decreasing only during the senescence when the climate is dryer and warmer and the soil moisture drops. As seen in the standard deviation values presented in Fig. 5d, EF remains rather constant during the daytime (between 08:00 and 12:00 UTC) for clear sky cases, allowing us the calculation of daily latent heat fluxes assuming the self-preservation of EF (Crago, 1996a,b). EF shows on the other hand a higher daytime variability during rainfall spells or highly variable

Table 4
Statistic discrepancies between predicted and observed measurements.

Platform/sensor	No. cases	RMSE	Bias	MAE	R^2	ANOVA p-value
Landsat5 TM	7	0.11	0.07	0.09	0.77	0.0053
Envisat AATSR/MERIS	18	0.15	0.02	0.11	0.41	0.0041
MSG SEVIRI	37	0.23	0.15	0.19	0.24	0.0022

Table 5
Statistic discrepancies between resampled Landsat imagery results (*Simple* and *Variable max VI*) and observed measurements.

Resampled resolution	No. cases	RMSE	Bias	MAE	R^2	ANOVA p-value
1 km	7	0.12	0.02	0.09	0.57	0.0485
4 km	7	0.25	0.20	0.21	0.33	0.1793

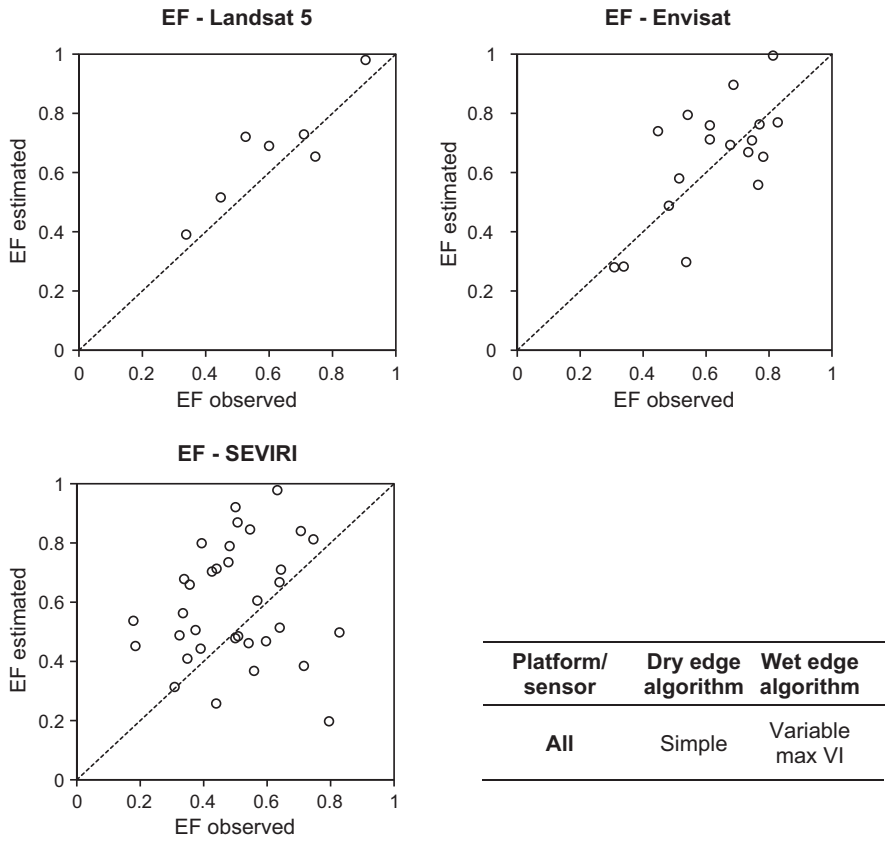

Fig. 8. Comparison of remotely sensed EF estimates, without applying a mask, with field measurements.

atmospheric forcing conditions, and therefore special care should be taken in those cases when extrapolating the instantaneous EF to daily ET.

Clearly, spatial resolution plays an important role in the triangle performance (Tables 4–7). Fig. 11 shows the T_s–VI scatterplots of the analyses carried out in Section 3.2 for two specific dates (4th April 2010 and 23rd June 2010). The scatterplots of the selected days differ between datasets. Firstly, the number of points (pixels) in the scatterplots obviously decreases as the sensors resolution does, forcing in some cases the use of a larger spatial domain with the risk of breaking the assumption of homogeneous atmospheric forcing. Secondly, while the dry edge generally adjusts fairly well to the triangular shape, the wet edge adjustment depends on the algorithm used. Some cases might be affected by undetected clouds and/or shadows, as in the case of Landsat low T_s/NDVI dispersed values under the wet edges in April.

Landsat statistics present better results than the other datasets. Moderate or low spatial resolution sensors fail to differentiate variations in T_s, VI and soil moisture conditions at field scales (Kustas et al., 2004; McCabe & Wood, 2006), therefore affecting the T_s–VI space and compromising results. Fig. 12 compares pixel sizes at the experimental site. While Landsat pixels mostly represent homogenous land cover types, the in-pixel landscape heterogeneity clearly increases for Envisat and, specially, SEVIRI pixels. Indeed, since our area is composed of many mosaics and patched vegetation, Envisat and SEVIRI pixels usually include a significant presence of bare soil, and hence the wet edge is warmer compared to the wet edge in Landsat (Fig. 11), where it is more likely to obtain pure pixels of vegetation and hence lower temperatures.

Most studies give no details of the window domain used, apparently applying the triangle over the entire image. Working on small tiles, i.e. running the algorithm on each tile independently, might improve results by working over more homogeneous conditions. In a recent research, Long et al. (2012) concluded that within the same dataset enlarging the domain size makes the observed dry and wet edge to move upward and downward, respectively, due to a broader range of soil moisture conditions present. As a consequence, effectiveness in their automatic establishment might decrease worsening the results. Uncertainties like these in determining the spatial domain of triangular models, suggest that a previous calibration is required (Long & Singh, 2013). That is the reason why several tests were carried out prior to our comparison to determine an optimal window size for each dataset. Analyses in Section 3.2.1 confirmed the displacement of the wet edge on Landsat imagery when using the *S. Mean* algorithm. However, such displacement of the wet edge was contrary when using *S. Var max VI*, as its establishment depends on the dry edge position.

Spatial resolution determines the size of the window domain, which might affect results as well. Although the triangle edges remain unaffected, some high LAI pixels outside the triangle borders must be noticed (4th April in Fig. 11c and 23rd June in Fig. 11d). The highest LAI values of Envisat in Fig. 11c correspond to scattered pixels in the area, whose value is diminished upon mixing with surrounding low values at the SEVIRI pixel resolution. As SEVIRI pixels are bigger, a larger

Table 6
Statistic discrepancies between predicted and observed measurements.

Platform/sensor	No. cases	RMSE	Bias	MAE	R^2	ANOVA p-value
Landsat5 TM	7	0.10	0.06	0.09	0.80	0.0030
Envisat AATSR/MERIS	18	0.15	0.02	0.12	0.46	0.0019
MSG SEVIRI	37	0.36	0.15	0.26	0.06	0.1294

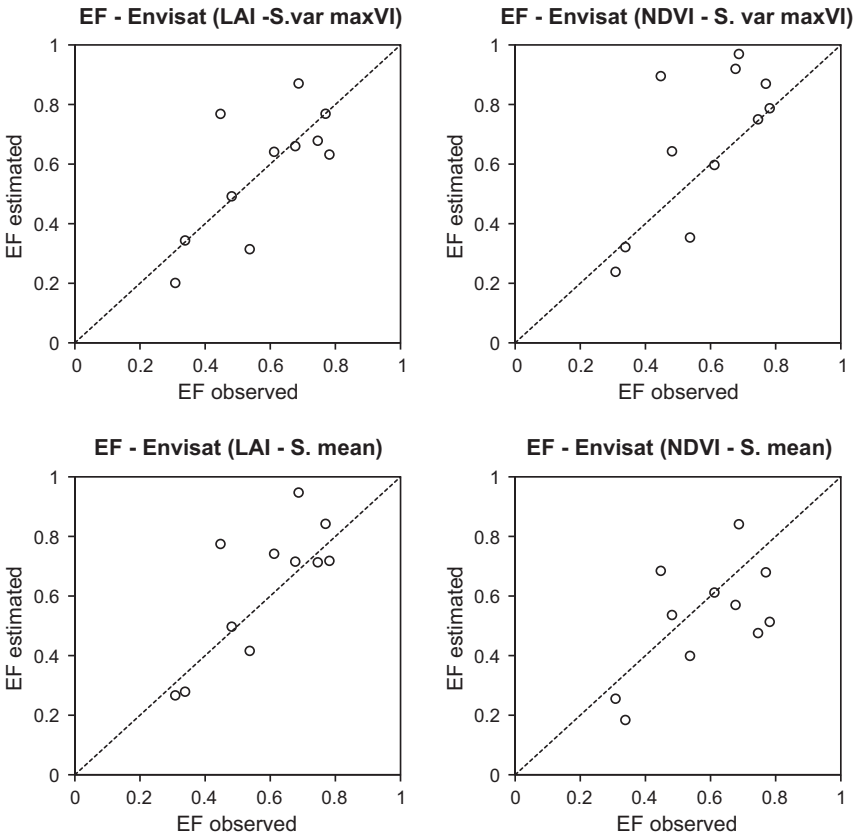

Fig. 9. Comparison of remotely sensed EF estimates, using LAI or NDVI as the vegetation index for the Envisat dataset, with field measurements.

window size is required, causing LAI values in Fig. 11d for June to be higher than those for the same date in Fig. 11c. In this case those values correspond to sunflower crops located out of the range of the Envisat spatial domain, which are growing at this time of the year in the region. Likewise, it must be considered that uncertainties in LAI products might lead to major errors in estimations. Equations in Fig. 11 denote an increase in temperature range between the two edges as the image resolution increases, as a consequence of the spatial resolution and window domain size.

Intra-pixel landscape heterogeneity and the number of pixels available within each domain are likely to be the sources of errors explaining worse edges adjustment and lower performance with Envisat and SEVIRI data. In particular, given the spatial resolution of SEVIRI, and in order to avoid a window domain where the assumption of homogeneous atmospheric forcing might no longer be valid, a rather small window of 60 × 60 km was selected. This issue leads then to having a rather small number of pixels (225 pixels) for calculating the dry and wet edges (see Fig. 11d) and a consequent reduced performance in the results for this sensor. Despite SEVIRI coarse resolution being unable to capture the spatial variability in fluxes where intra-pixel heterogeneity is present, it successfully estimates average fluxes at large scale (Stisen et al., 2008). Although working with finer resolutions has shown to produce better results, it usually compromises other aspects, such as radiometric and temporal resolutions in Landsat. Having multitemporal observations as in the case of SEVIRI might be an advantage, however, working with such a pixel size over heterogeneous or scattered vegetated areas becomes a difficult task. Despite not using dT_s in our analysis, our SEVIRI results are consistent with previous results (Shu et al., 2011; Stisen et al., 2008). Additional work should include further research on applying T_s difference over heterogeneous areas, due to its usefulness for this type of models.

Furthermore, as McCabe and Wood (2006) pointed out, a comparison of remote sensing retrievals with field measurements entails an inadequate validation assessment, due to factors such as representativeness of the validation point within the sensor pixel resolution, sensor measurements accuracy and/or physically discrepancies between measured and observed variables (time averaged atmospheric boundary-layer measurements compared with instantaneous empirically based estimations). Regarding the first factor, Table 5 shows the evaluation of the representativeness of the validation site at Envisat and SEVIRI scales. Statistical discrepancies indicated that the size of the experimental field, while being appropriate for Envisat, might not be representative within the SEVIRI pixel size. The no statistically significant ANOVA relation between observed measurements and Landsat results aggregated to 4 km is a consequence of the sub-pixel variability of EF estimates at SEVIRI scale, which leads to an inefficient effort for a validation strategy. Consequently, the scale mismatch between SEVIRI pixel size and scintillometer footprint is likely to explain most of the lower performance in EF estimations.

Similarly, the importance of the deployment and location of the validation equipment has to be considered, especially in heterogeneous areas, where enough validation sites for distinguishing between different vegetation classes should ideally be present (Long & Singh, 2013; McCabe & Wood, 2006). In the absence of such a validation network for this study, our validation equipment was placed on a non-irrigated winter crop, for being a dominant vegetation class in the study area.

Table 7
Statistic discrepancies between predicted and observed measurements.

Method	No. cases	Vegetation index	RMSE	Bias	MAE	R^2	ANOVA p-value
LAI	11	*S. Var max VI*	0.14	0.00	0.10	0.51	0.0135
	11	*S. Mean*	0.14	0.05	0.11	0.62	0.0040
NDVI	11	*S. Var max VI*	0.19	0.09	0.14	0.52	0.0128
	11	*S. Mean*	0.16	−0.06	0.14	0.38	0.0452

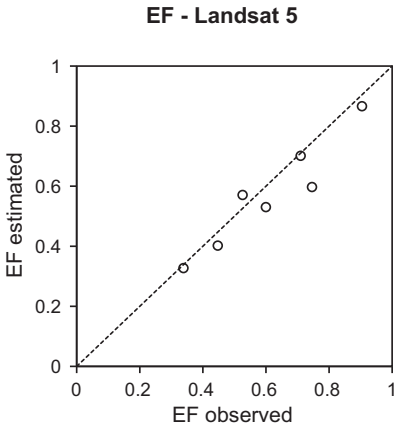

Platform/ sensor	Dry edge algorithm	Wet edge algorithm
Landsat5 TM	Tang	Variable max VI

Fig. 10. Comparison of remotely sensed EF estimates from Landsat, using the *Tang* algorithm for the dry edge, with field measurements.

The relative position of the validation pixels within the boundaries of the triangle is significant for triangular models, especially when considering issues related to the establishment of the edges, as commented before. As seen in Fig. 13, when both edges move in opposite directions (dry edge 1 to dry edge 2, and wet edge 1 to wet edge 2) due to increasing domain size or uncertainties in the derivation of them, EF estimates from pixels distributed in the central T_s/VI space of each VI interval (i_1) remain relatively invariant, while EF estimations from pixels close to the edges (i_2) are likely to present significant changes (see equations in Fig. 13). Therefore, validation pixels centrally distributed would reduce the effects of resolution or domain dependencies, leading to a reduced utility of the validation effort. However, these kind of issues are mainly related to changes of domain size within the same satellite imagery (dataset), and not to changes associated with the enlargement of the domain size due to image resolution (i.e. coarser resolutions require larger domains), as the changes observed in EF would be consequences not only of the former, but also of the intra-pixel heterogeneity associated to coarser pixels as commented before. At the same time, central pixels might be considered robust for providing an average performance of the model.

As the *S. Var max VI* algorithm showed no such issue, meaning that the location of the validation site in this study was eligible for providing effective measurements of EF under extreme conditions, it was selected for the dataset model comparison analysis in Section 3.2.2, avoiding a biased validation attempt. And so, our results are in accordance with previous findings, such as the scale dependencies found by Long et al. (2012) comparing Landsat TM/ETM+ with MODIS EF estimates on the Soil Moisture–Atmosphere Coupling Experiment (SMACEX) site in central Iowa (USA). They concluded as well that using their proposed trapezoid model with theoretical limiting edges can constrain domain and resolution dependencies to some extent.

To our knowledge, masking terrain conditions is not a commonly discussed issue on triangle applications. Merely some topographical information for the interpolation of T_a has been integrated on previous works (Ishimura, Shimizu, Rahimzadeh-Bajgiran, & Omasa, 2011). With our analyses we show the importance of such step when applying this kind of methods, especially over low resolution imagery. As seen in the results, SEVIRI RMSE almost doubles without applying a mask. This can be explained by the comparatively higher presence of masked categories within the larger SEVIRI domain, in contrast with Landsat and Envisat, corresponding not only to vegetation types with significant differences in roughness, but also to larger altitude range and slopes. In fact, the percentages of masked pixels within the Landsat, Envisat and SEVIRI's domains are around 20%, 27% and 45%, respectively.

Table 8
Statistic discrepancies between predicted and observed measurements.

Platform/sensor	No. cases	RMSE	Bias	MAE	R^2	ANOVA p-value
Landsat5 TM	7	0.07	−0.04	0.05	0.90	0.0030

In general, NDVI/LAI values in Fig. 11 are higher in April than in June, as the latter corresponds to the senescence period. Hence, the triangular shape is better defined in June, when more soil moisture conditions can be found within the image due to water stress. Mostly, the equations are in agreement with the statistics presented before. Landsat NDVI maximum values (Fig. 11a) are higher than those for Envisat (Fig. 11b) due to not only different pixel sizes and window domains, but also different spectral responses. While NDVI is just a surface greenness indicator, LAI is a physical parameter whose magnitude better represents the surface reality. Therefore, as expected, the triangle results improved using the latter in the T_s–VI space. Previous studies have used similar indexes, such as the Fractional Vegetation Cover (Jiang & Islam, 2003; Nishida et al., 2003) but none was found using LAI, nor comparing results between different indexes.

Regarding the triangle limits, as seen in Figs. 11 and 14, the dry edge is generally better defined than the wet edge, both for NDVI and LAI. Therefore, it can be concluded that the use of the non-linear ϕ_{min} interpolation from Stisen et al. (2008) can be feasible when working with either NDVI or LAI. Usually, triangle methods assume that full-cover vegetation is not undergoing water stress, meaning that the vegetation temperature does not get significantly larger than the minimum temperature. This kind of interpolation can be seen as a proxy for allowing some degree of water stress, by minimizing the difference between the true dry edge and the observed dry edge. The *Tang* algorithm was found to be applicable only to Landsat imagery due to higher pixel resolution and the larger number of pixels within the domain. The algorithm, which divides the range of VI in the triangle space into intervals and subintervals, did not properly work for coarser sensors like Envisat and SEVIRI that are unable to discriminate small VI variations. Therefore only the *Simple method* was used with Envisat and SEVIRI. Results were improved in the case of Landsat by applying both *Tang* and *Var max VI* algorithms (Section 3.2.5), due to a better definition of the dry edge and the dependency that the *Var max VI* wet edge has on a correct characterization of the dry edge.

The saturation of NDVI at higher LAI values – and hence at dense vegetation – shown in Fig. 2a, is confirmed in the Landsat triangles of Fig. 11a. In this case, the value of the *Var max VI* wet edge, as it intersects with the maximum VI value of the dry edge, is quite higher than the value of *Mean* wet edge, and usually removes from the triangle the areas highlighted in Fig. 15. This effect is also observed in the case of Envisat when using NDVI (Fig. 11b). On the contrary, when using LAI

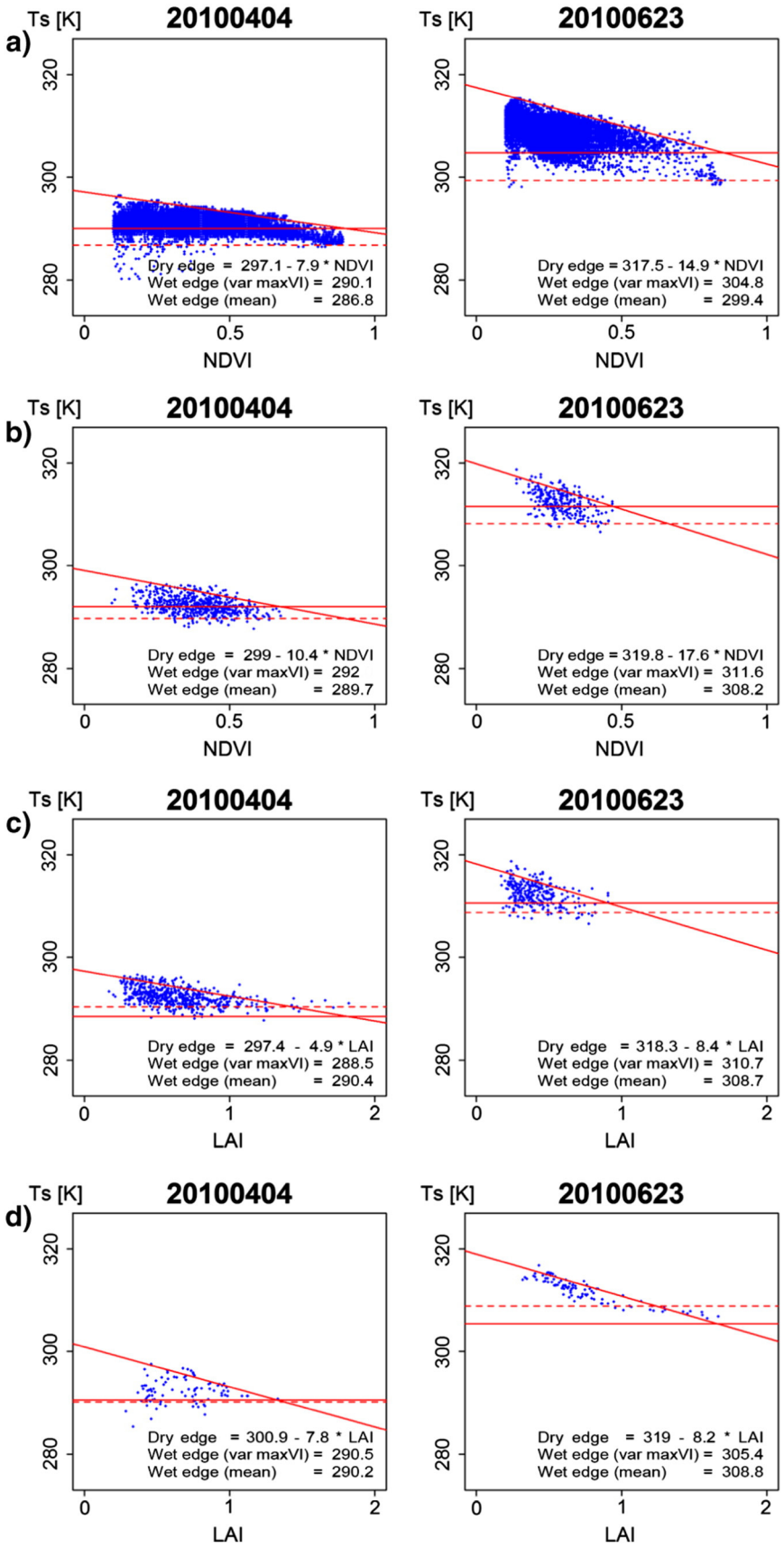

Fig. 11. Scatterplots of the triangles for all datasets, using *Simple* algorithm for the dry edge and *Var max VI* (horizontal solid line) or *Mean* (horizontal dashed line) algorithms for the wet edge, respectively: a) Landsat; b) Envisat-NDVI; c) Envisat-LAI; d) SEVIRI.

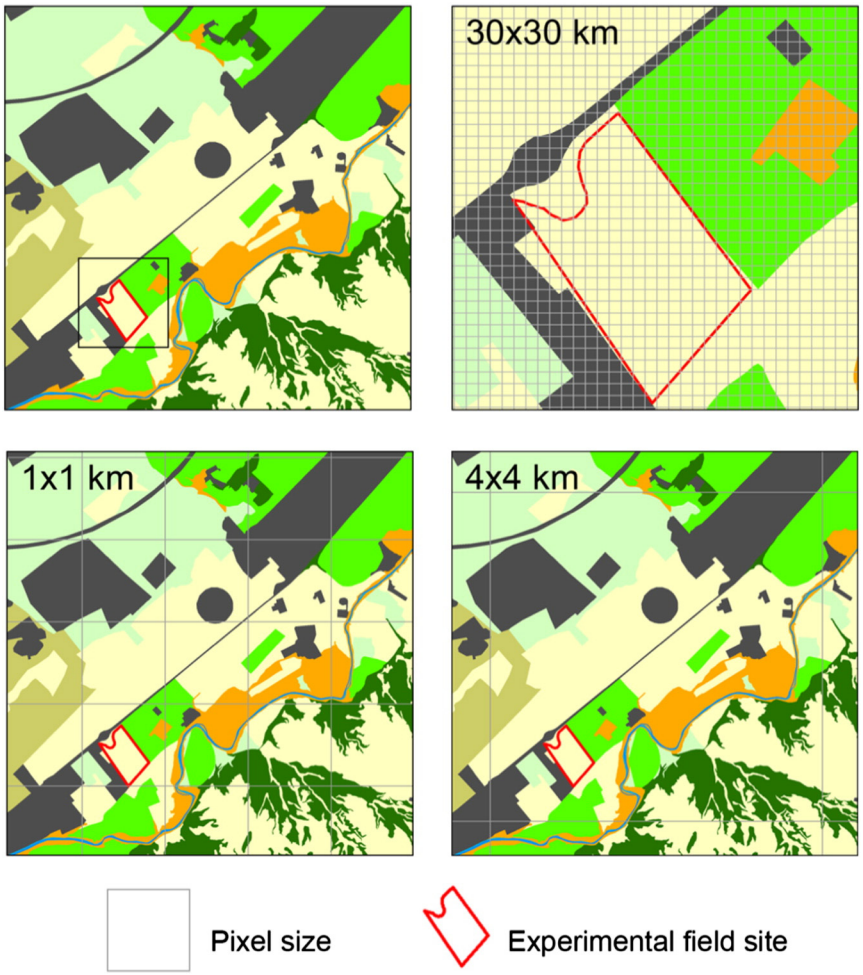

Fig. 12. Pixel size comparison at the experimental site: Landsat5-TM (30 m), Envisat (1 km), SEVIRI (4 km). (For a better interpretation of the colors in this figure, the reader is referred to the web version of this article.)

(Fig. 11c) the *Var max VI* wet edge is usually lower than the *Mean* wet edge and hence it seems to better adapt to the expected theoretical wet edge. Fig. 14 shows the scatterplots of the triangles for the Envisat images, both using NDVI and LAI in the T_s/VI space. From this figure, the *Var max VI* algorithm generally represents better the wet edge when using LAI as the vegetation index, while *Mean* performs better for NDVI. It is worth noting that although Han et al. (2006) stated that NDVI saturates with LAI above 6, we have observed that the T_s/VI space seems better defined using LAI in our study, despite our LAI values never reaching up to 3. Based on simulations using the coupled radiative transfer model PROSPECT (Jacquemoud & Baret, 1990) and 4SAIL (Verhoef et al., 2007), we have plotted LAI and NDVI in Fig. 16, confirming that NDVI can saturate (NDVI ~ 1) even with LAI values as low as 1, depending obviously on the spectral response function of the sensor.

When using NDVI as the vegetation index, the scatterplots of Landsat and Envisat (Fig. 11a–b) show a better representation of the wet edge by the *Mean* algorithm, which is confirmed by the Envisat statistics in Section 3.2.4 and scatterplots of Fig. 14. We made some analyses applying the *Mean* algorithm to Landsat. However resultant EF indicated worse statistics than the one found with *Var max VI*, probably because the T_s min obtained with the latter is closer to the T_s of the experimental field at the acquisition time. In fact, the Landsat pixels located between the two wet edges in the T_s/VI space correspond to areas with presumably higher water content, due to either irrigation or rainfall. Fig. 15 highlights those pixels for Landsat NDVI images on the same two dates as Fig. 11a. In comparison to the land cover map detail (Fig. 12, 30 × 30 m) the highlighted pixels mainly correspond to irrigated crops close to the river. There are, as well, some other residual non-irrigated areas at the bottom right corner, which probably keep moisture due to uneven terrain conditions.

In the same way, whenever LAI is used, the *Var max VI* algorithm seems to work slightly better according to the Envisat statistics in Section 3.2.4 and scatterplots of Figs. 11c–d and 14. The Envisat scatterplot for the 23rd of June seems to be a clear exception and it is explained by the same reason as mentioned before for the Landsat cases, i.e. presence of irrigated areas. Still, further research needs to be done in comparing algorithms to investigate this issue, since an adequate establishment of the edges is essential for a good performance of the triangle method.

Finally, the Ts min in the *Var max VI* is taken as the value of the dry edge at a value of NDVI = 0.9 or LAI = 1.9, representing full vegetation cover, or at the actual maximum value of NDVI/LAI in the image, whichever is smaller in order to not incur the overestimation of the wet edge. This derivation of the wet edge might suffer from subjectivity when choosing those VI values. Tang et al. (2010) propose to build the triangle with the fractional cover (which is more physically-based than a simple VI). However, *fc* is usually estimated based on empirical approaches that scale the NDVI from a NDVI max and min such as in Tang et al. (2010), thus also suffering from subjectivity. We consider therefore that it is equally arbitrary to use max NDVI in the VI–Ts space as it is to use it (NDVI max = 0.86 in case of Tang, based on Prihodko and Goward (1997)) for estimating *fc*. Furthermore maximum cover NDVI values are species specific and, more important, any vegetation index is sensor specific (Prihodko and Goward (1997) uses AVHRR

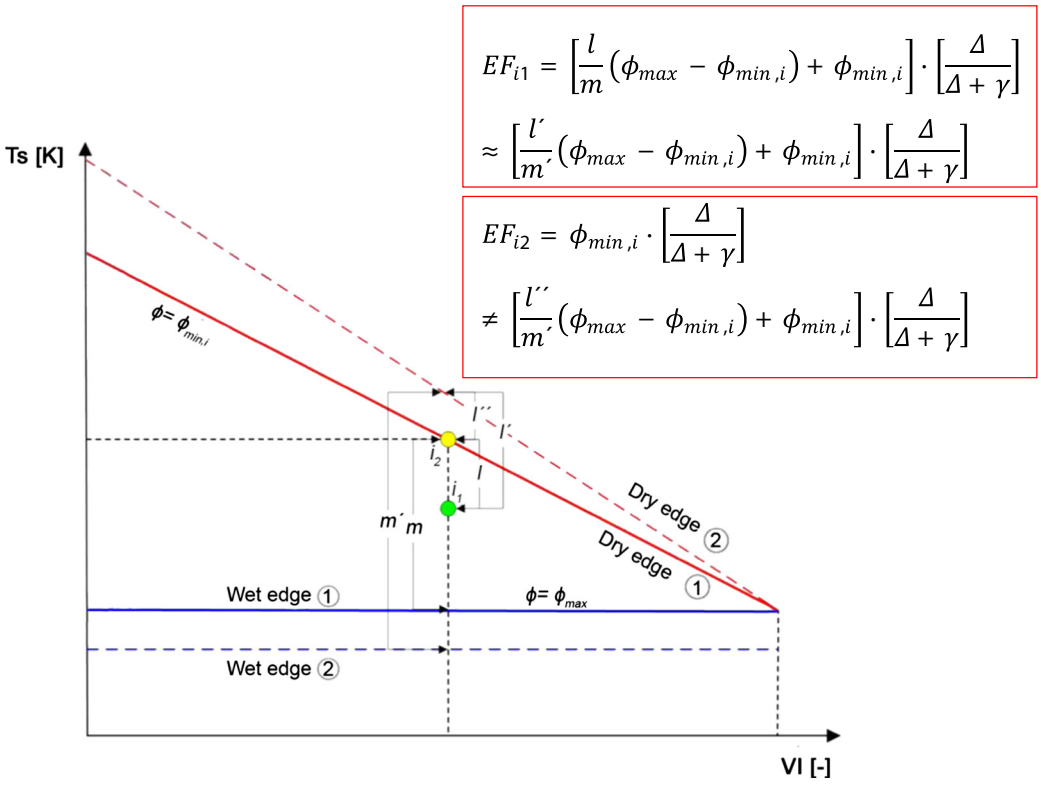

Fig. 13. Effect of the relative position of pixels in triangle models associated to domain dependencies, adapted from Long and Singh (2013). Point i_1 represents a pixel centrally located within the T_s/VI space, and point i_2 represents a pixel located close to the dry edge. Distance l represents the difference in T_s between point i_1 and the dry edge 1. Distance l' represents the difference in T_s between point i_1 and the dry edge 2. Distance l'' represents the difference in T_s between point i_2 and the dry edge 2. Distance m represents the difference in T_s between the wet edge 1 and the dry edge 1. Distance m' represents the difference in T_s between the wet edge 2 and the dry edge 2.

while Tang et al. (2010) apply the same value for MODIS) as discussed by Stisen, Sandholt, Nørgaard, Fensholt, and Eklundh (2007) and Nieto et al. (2011).

5. Conclusions

This study has evaluated the triangle approach for estimating EF over a heterogeneous area, focusing on four main issues that can affect the model performance: pixel resolution, terrain conditions (vegetation classes, altitude, slope), vegetation index, and edge algorithms used. To achieve this, satellite imagery with different spatial resolution were used (MSG-SEVIRI, Envisat-AATSR/MERIS and Landsat5-TM); the influence of terrain conditions was verified by developing a mask; NDVI and LAI were analyzed as the vegetation index; and different combinations of the wet and dry edge algorithms were tested.

Our analyses shed light on how results are indeed affected by those aspects. Finer satellite resolution results in better performance, usually compromising the temporal resolution. Topographic heterogeneity negatively affects results, making it necessary to use masks for ensuring, as far as possible, uniform terrain conditions, whenever the number of remaining pixels can provide an appropriate definition of the triangular shape. And finally, results depend as well on the type of vegetation index used, working better with LAI than NDVI due to saturation effects, and edge algorithms, being more adequate *Var max VI* for LAI and *Mean* for NDVI.

Applying the triangle method entails a main limitation to consider, which is the large number of pixels required within an image with a wide range of soil moisture and fractional vegetation cover conditions. Wet surfaces evaporating at potential rates, as well as dry surfaces where almost no ET occurs, are necessary. As demonstrated and in agreement with previous studies (Long & Singh, 2012; Long et al., 2012), results are dependent on domain size and pixel resolution. Thus, a prior calibration for selecting a proper window domain becomes a non-trivial but decisive task, and it will depend on the sensor used and the nature of the area of interest. In the same way, representativeness of the validation site is critical for an accuracy assessment, and the deployment and location of the validation equipment must be carefully selected.

Some intrinsic assumptions to the triangular shape need to be made as well (Long & Singh, 2012). For instance, 1) due to the model's one-source scheme, the triangle is not able to discriminate vegetation transpiration from soil surface evaporation — the latter may reduce the overall evaporative demand by decreasing the air vapor pressure deficit and therefore might affect the vegetation water use; 2) the aerodynamic and physiological effects of the surface on sensible heat flux are not explicitly taken into account, but are assumed to be explained within the NDVI–T_s space — indeed as we have demonstrated, landscape heterogeneity affects results; 3) it is assumed there is a non-linear variation of EF across the VI–T_s space; and 4) certain level of subjectivity is frequently involved when establishing both edges, and the type of algorithm used affects results — the wet edge in particular is often affected by pixels with low values of VI and T_s (e.g. clouds, slopes, shadows) which deform the triangle shape at its base, making its determination more difficult.

Nonetheless, and as summarized by Tang et al. (2010), the triangle approach presents several advantages. In particular, 1) as results are based on the relative position of pixels within the triangle and not on highly accurate T_s retrievals, sophisticated atmospheric corrections are not required; 2) since ϕ is a replacement for the aerodynamic term, there is no need for its complex parameterization, avoiding in this way uncertainties introduced by replacing aerodynamic temperature by remotely sensed T_s; 3) apart from T_s and VI, no other satellite retrievals are necessary; 4) EF is directly and independently obtained, with no need of estimating any other component of the surface energy

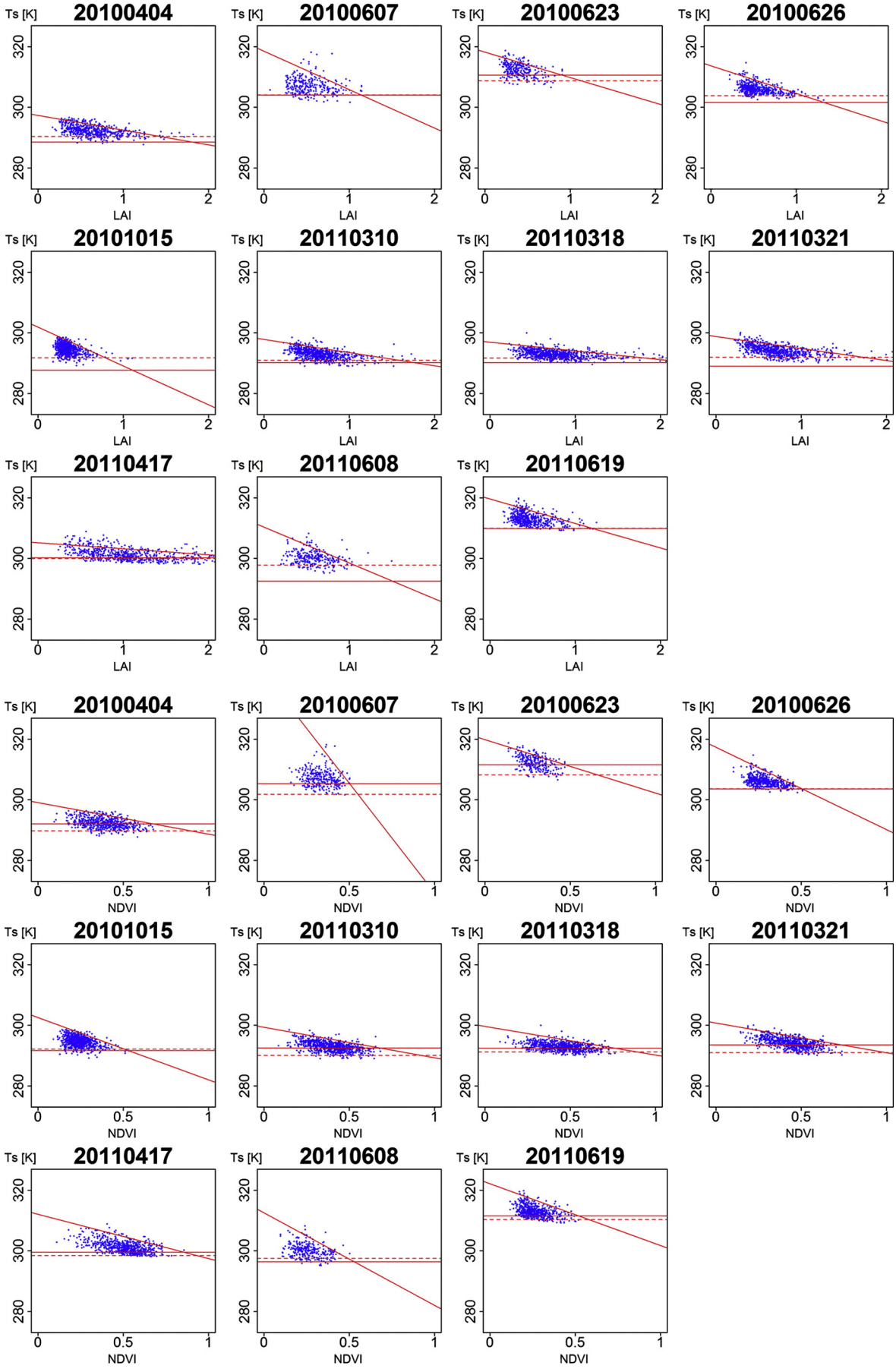

Fig. 14. Scatterplots of the Envisat triangles for the NDVI/LAI comparison analysis. Horizontal line represents the wet edge estimated by *Var max VI* (solid) or *Mean* (dashed).

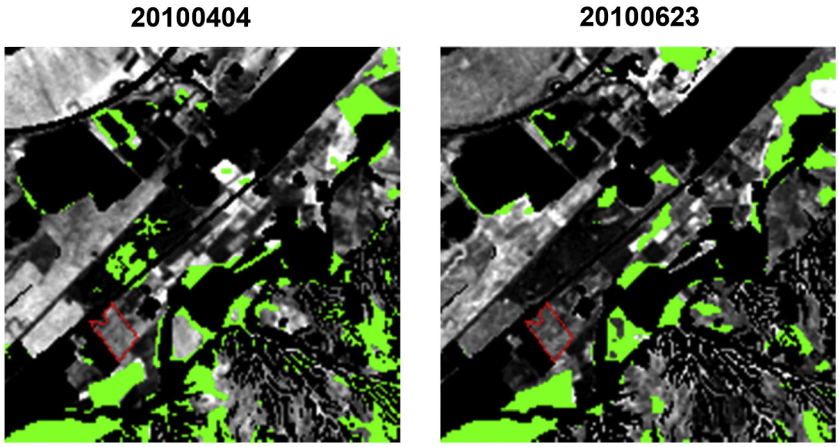

Fig. 15. In green, pixels located between *Mean* and *Var max VI* wet edges in the T_s/VI space of two Landsat images. For the visualization of the triangles see Fig. 11a. (For interpretation of the references to color in this figure legend, the reader is referred to the web version of this article.)

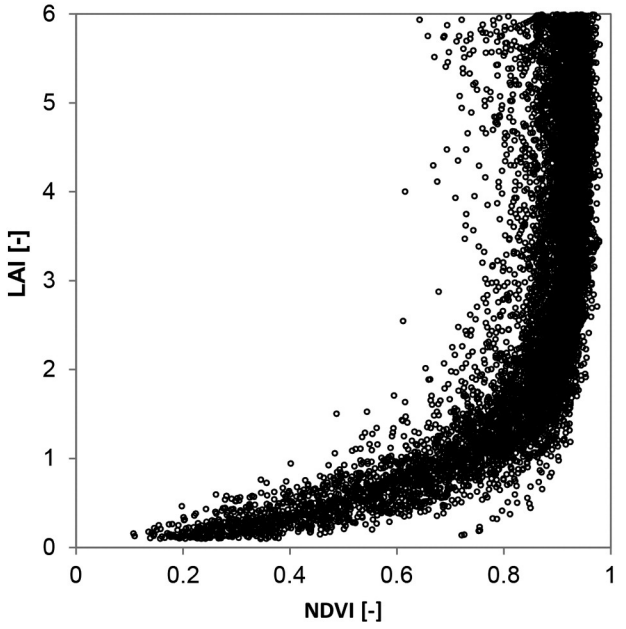

Fig. 16. Scatterplot of LAI vs. NDVI based on 20,000 random simulations using PROSPECT + 4SAIL.

balance component; and 5) consequently to the latter, errors in ET estimations can be independently traced back.

In summary, regardless model intrinsic assumptions, its simplicity and reasonably good performance make the triangle a considerable choice among other methodologies. Despite the lack of more field observations for a regional validation, the methodology presented here is considered to be independent of the local measurements and applicable for estimating EF at regional scales, including heterogeneous areas. Additional work on improving operability, by obtaining frequent EF estimations at high resolution by combining different satellite imagery, will be the basis of future research.

Acknowledgments

This research was initialized during a visiting stay at the Department of Geosciences and Natural Resource Management of the University of Copenhagen, Denmark, thanks to a grant within the BACH project funded by IMDEA Water Institute. This study is likewise part of the INTEGRATOR Project (CTM2011-27657) funded by the Spanish Ministry of Science and Innovation. The authors would like to thank the Spanish National Institute for Agricultural and Food Research and Technology (INIA), especially to the workers of La Canaleja, for allowing us to carry on ground measurements at their site and making things easier. We would also like to thank the constructive comments from the anonymous reviewers, which helped to improve the final version of the manuscript.

References

Allen, R., Tasumi, M., & Trezza, R. (2007). Satellite-based energy balance for mapping evapotranspiration with internalized calibration (METRIC) — Model. *Journal of Irrigation and Drainage Engineering, 133*, 380–394.

Anderson, M. C., Norman, J. M., Diak, G. R., Kustas, W. P., & Mecikalski, J. R. (1997). A two-source time-integrated model for estimating surface fluxes using thermal infrared remote sensing. *Remote Sensing of Environment, 60*, 195–216.

Baret, F., Bacour, C., Beal, D., Weiss, M., Berthelot, B., & Regner, P. (2006). Algorithm theoretical basis document for MERIS top of atmosphere land products (TOA_VEG). *INRA — Novelties*.

Bastiaanssen, W. G. M., Menenti, M., Feddes, R. A., & Holtslag, A. A.M. (1998). A remote sensing surface energy balance algorithm for land (SEBAL). 1. Formulation. *Journal of Hydrology, 212–213*, 198–212.

Bastiaanssen, W. G. M., Thiruvengadachari, S., Sakthivadivel, R., & Molden, D. J. (1999). Satellite remote sensing for estimating productivities of land and water. *International Journal of Water Resources Development, 15*, 181–194.

Batra, N., Islam, S., Venturini, V., Bisht, G., & Jiang, L. (2006). Estimation and comparison of evapotranspiration from MODIS and AVHRR sensors for clear sky days over the Southern Great Plains. *Remote Sensing of Environment, 103*, 1–15.

Carlson, T. (2007). An overview of the "triangle method" for estimating surface evapotranspiration and soil moisture from satellite imagery. *Sensors, 7*, 1612–1629.

Carlson, T. N., Capehart, W. J., & Gillies, R. R. (1995). A new look at the simplified method for remote sensing of daily evapotranspiration. *Remote Sensing of Environment, 54*, 161–167.

Carlson, T. N., Gillies, R. R., & Schmugge, T. J. (1995). An interpretation of methodologies for indirect measurement of soil water content. *Agricultural and Forest Meteorology, 77*, 191–205.

Caselles, V., Valor, E., Coll, C., & Rubio, E. (1997). Thermal band selection for the PRISM instrument 1. Analysis of emissivity–temperature separation algorithms. *Journal of Geophysical Research, 102*, 11145–11164.

Chander, G., Markham, B.L., & Helder, D. L. (2009). Summary of current radiometric calibration coefficients for Landsat MSS, TM, ETM+, and EO-1 ALI sensors. *Remote Sensing of Environment, 113*, 893–903.

Chauhan, N. S., Miller, S., & Ardanuy, P. (2003). Spaceborne soil moisture estimation at high resolution: A microwave–optical/IR synergistic approach. *International Journal of Remote Sensing, 24*, 4599–4622.

Chavez, P.S. (1996). Image-based atmospheric corrections. Revisited and improved. *Photogrammetric Engineering and Remote Sensing, 62*, 1025–1036.

Crago, R. D. (1996a). Comparison of the evaporative fraction and the Priestley–Taylor α for parameterizing daytime evaporation. *Water Resources Research, 32*, 1403–1409.

Crago, R. D. (1996b). Conservation and variability of the evaporative fraction during the daytime. *Journal of Hydrology, 180*, 173–194.

Crago, R., & Brutsaert, W. (1996). Daytime evaporation and the self-preservation of the evaporative fraction and the Bowen ratio. *Journal of Hydrology, 178*, 241–255.

Fensholt, R., Sandholt, I., Stisen, S., & Tucker, C. (2006). Analysing NDVI for the African continent using the geostationary Meteosat second generation SEVIRI sensor. *Remote Sensing of Environment, 101*, 212–229.

French, R., & Schultz, J. (1984). Water use efficiency of wheat in a Mediterranean-type environment. I. The relation between yield, water use and climate. *Australian Journal of Agricultural Research*, *35*, 743–764.
Garcia-Haro, F. J., Fernando Camacho-de, C., & Melia, J. (2006). A directional spectral mixture analysis method: Application to multiangular airborne measurements. *IEEE Transactions on Geoscience and Remote Sensing*, *44*, 365–377.
Gillies, R. R., Kustas, W. P., & Humes, K. S. (1997). A verification of the 'triangle' method for obtaining surface soil water content and energy fluxes from remote measurements of the Normalized Difference Vegetation Index (NDVI) and surface e. *International Journal of Remote Sensing*, *18*, 3145–3166.
Goward, S. N., Waring, R. H., Dye, D.G., & Yang, J. (1994). Ecological remote sensing at OTTER: Satellite macroscale observations. *Ecological Applications*, *4*, 322–343.
Gutiérrez-Elorza, M., García-Ruiz, J. M., Goy, J. L., Gracia, F. J., Gutiérrez-Santolalla, F., Martí, C., et al. (2002). Quaternary. In W. Gibbons, & T. Moreno (Eds.), *The geology of Spain*. Bath, UK: Geological Society of London.
Guzinski, R., Anderson, M. C., Kustas, W. P., Nieto, H., & Sandholt, I. (2013). Using a thermal-based two source energy balance model with time-differencing to estimate surface energy fluxes with day–night MODIS observations. *Hydrology and Earth System Sciences*, *17*, 2809–2825.
Ha, W., Gowda, P., & Howell, T. (2012). A review of downscaling methods for remote sensing-based irrigation management: Part I. *Irrigation Science*, *1–20*.
Han, L., Wang, P., Yang, H., Liu, S., & Wang, J. (2006). Study on NDVI-Ts space by combining LAI and evapotranspiration. *Science in China Series D: Earth Sciences*, *49*, 747–754.
Hill, R. J. (1992). Review of optical scintillation methods of measuring the refractive-index spectrum, inner scale and surface fluxes. *Waves in Random Media*, *2*, 179–201.
Ishimura, A., Shimizu, Y., Rahimzadeh-Bajgiran, P., & Omasa, K. (2011). Remote sensing of Japanese beech forest decline using an improved Temperature Vegetation Dryness Index (iTVDI). *iForest — Biogeosciences and Forestry*, *4*, 195–199.
Jacquemoud, S., & Baret, F. (1990). PROSPECT: A model of leaf optical properties spectra. *Remote Sensing of Environment*, *34*, 75–91.
Jiang, L., & Islam, S. (1999). A methodology for estimation of surface evapotranspiration over large areas using remote sensing observations. *Geophysical Research Letters*, *26*, 2773–2776.
Jiang, L., & Islam, S. (2001). Estimation of surface evaporation map over Southern Great Plains using remote sensing data. *Water Resources Research*, *37*, 329–340.
Jiang, L., & Islam, S. (2003). An intercomparison of regional latent heat flux estimation using remote sensing data. *International Journal of Remote Sensing*, *24*, 2221.
Kustas, W. P., Choudhury, B. J., Moran, M. S., Reginato, R. J., Jackson, R. D., Gay, L. W., et al. (1989). Determination of sensible heat flux over sparse canopy using thermal infrared data. *Agricultural and Forest Meteorology*, *44*, 197–216.
Kustas, W. P., Li, F., Jackson, T. J., Prueger, J. H., MacPherson, J. I., & Wolde, M. (2004). Effects of remote sensing pixel resolution on modeled energy flux variability of croplands in Iowa. *Remote Sensing of Environment*, *92*, 535–547.
Kustas, W. P., Perry, E. M., Doraiswamy, P. C., & Moran, M. S. (1994). Using satellite remote sensing to extrapolate evapotranspiration estimates in time and space over a semiarid Rangeland basin. *Remote Sensing of Environment*, *49*, 275–286.
Lambin, E. F., & Ehrlich, D. (1996). The surface temperature–vegetation index space for land cover and land-cover change analysis. *International Journal of Remote Sensing*, *17*, 463–487.
Li, Z. -L., Jia, L., Su, Z., Wan, Z., & Zhang, R. (2003). A new approach for retrieving precipitable water from ATSR2 split-window channel data over land area. *International Journal of Remote Sensing*, *24*, 5095–5117.
Long, D., & Singh, V. P. (2012). A two-source trapezoid model for evapotranspiration (TTME) from satellite imagery. *Remote Sensing of Environment*, *121*, 370–388.
Long, D., & Singh, V. P. (2013). Assessing the impact of end-member selection on the accuracy of satellite-based spatial variability models for actual evapotranspiration estimation. *Water Resources Research*, *49*, 2601–2618.
Long, D., Singh, V. P., & Scanlon, B. R. (2012). Deriving theoretical boundaries to address scale dependencies of triangle models for evapotranspiration estimation. *Journal of Geophysical Research*, *117*.
Margulis, S. A., Kim, J., & Hogue, T. (2005). A comparison of the triangle retrieval and variational data assimilation methods for surface turbulent flux estimation. *Journal of Hydrometeorology*, *6*, 1063–1072.
McCabe, M. F., & Wood, E. F. (2006). Scale influences on the remote estimation of evapotranspiration using multiple satellite sensors. *Remote Sensing of Environment*, *105*, 271–285.
Merlin, O. (2013). An original interpretation of the wet edge of the surface temperature–albedo space to estimate crop evapotranspiration (SEB-1S), and its validation over an irrigated area in northwestern Mexico. *Hydrology and Earth System Sciences*, *17*, 3623–3637.
Montetih, J. L (1965). Evaporation and the environment. *Proceedings of the 19th Symposium of the Society of Experimental Biology* (pp. 205–234). Cambridge University Press.
Moran, M. S., Clarke, T. R., Inoue, Y., & Vidal, A. (1994). Estimating crop water deficit using the relation between surface–air temperature and spectral vegetation index. *Remote Sensing of Environment*, *49*, 246–263.
Moran, M. S., Clarke, T. R., Kustas, W. P., Weltz, M., & Amer, S. A. (1994). Evaluation of hydrologic parameters in a semiarid rangeland using remotely sensed spectral data. *Water Resources Research*, *30*, 1287–1297.
Nieto, H., Sandholt, I., Aguado, I., Chuvieco, E., & Stisen, S. (2011). Air temperature estimation with MSG-SEVIRI data: Calibration and validation of the TVX algorithm for the Iberian Peninsula. *Remote Sensing of Environment*, *115*, 107–116.
Nishida, K., Nemani, R. R., Running, S. W., & Glassy, J. M. (2003). An operational remote sensing algorithm of land surface evaporation. *Journal of Geophysical Research, [Atmospheres]*, *108* (n/a–n/a).
Norman, J. M., Anderson, M. C., Kustas, W. P., French, A. N., Mecikalski, J., Torn, R., et al. (2003). Remote sensing of surface energy fluxes at 101-m pixel resolutions. *Water Resources Research*, *39* (n/a–n/a).
Norman, J. M., Kustas, W. P., & Humes, K. S. (1995). Source approach for estimating soil and vegetation energy fluxes in observations of directional radiometric surface temperature. *Agricultural and Forest Meteorology*, *77*, 263–293.
Owen, T. W., Carlson, T. N., & Gillies, R. R. (1998). An assessment of satellite remotely-sensed land cover parameters in quantitatively describing the climatic effect of urbanization. *International Journal of Remote Sensing*, *19*, 1663–1681.
Plummer, S. E. (2008). The GLOBCARBON cloud detection system for the along-track scanning radiometer (ATSR) sensor series. *IEEE Transactions on Geoscience and Remote Sensing*, *46*, 1718–1727.
Price, J. C. (1990). Using spatial context in satellite data to infer regional scale evapotranspiration. *IEEE Transactions on Geoscience and Remote Sensing*, *28*, 940–948.
Priestley, C., & Taylor, R. (1972). On the assessment of surface heat flux and evaporation using large-scale parameters. *Monthly Weather Review*, *100*, 81–92.
Prihodko, L., & Goward, S. N. (1997). Estimation of air temperature from remotely sensed surface observations. *Remote Sensing of Environment*, *60*, 335–346.
Rasmussen, M.O., Pinheiro, A.C., Proud, S. R., & Sandholt, I. (2010). Modeling angular dependences in land surface temperatures from the SEVIRI instrument onboard the geostationary Meteosat second generation satellites. *IEEE Transactions on Geoscience and Remote Sensing*, *48*, 3123–3133.
Roujean, J. -L., & Lacaze, R. (2002). Global mapping of vegetation parameters from POLDER multiangular measurements for studies of surface–atmosphere interactions: A pragmatic method and its validation. *Journal of Geophysical Research*, *107*, 4150.
Rouse, J., Harrs, R., Schell, J., Deering, D., & Harlan, J. (1974). *Monitoring the vernal advancement and retro gradation (green wave effect) of natural vegetation*. Greenbelt, MD, USA: NASA/GSFC.
Sandholt, I., Rasmussen, K., & Andersen, J. (2002). A simple interpretation of the surface temperature/vegetation index space for assessment of surface moisture status. *Remote Sensing of Environment*, *79*, 213–224.
Senay, G., Budde, M., Verdin, J., & Melesse, A. (2007). A coupled remote sensing and simplified surface energy balance approach to estimate actual evapotranspiration from irrigated fields. *Sensors*, *7*, 979–1000.
Shu, Y., Stisen, S., Jensen, K. H., & Sandholt, I. (2011). Estimation of regional evapotranspiration over the North China Plain using geostationary satellite data. *International Journal of Applied Earth Observation and Geoinformation*, *13*, 192–206.
Sobrino, J. A., Jiménez-Muñoz, J. C., & Verhoef, W. (2005). Canopy directional emissivity: Comparison between models. *Remote Sensing of Environment*, *99*, 304–314.
Sòria, G., & Sobrino, J. A. (2007). ENVISAT/AATSR derived land surface temperature over a heterogeneous region. *Remote Sensing of Environment*, *111*, 409–422.
Stisen, S., Sandholt, I., Nørgaard, A., Fensholt, R., & Eklundh, L. (2007). Estimation of diurnal air temperature using MSG SEVIRI data in West Africa. *Remote Sensing of Environment*, *110*, 262–274.
Stisen, S., Sandholt, I., Nørgaard, A., Fensholt, R., & Jensen, K. H. (2008). Combining the triangle method with thermal inertia to estimate regional evapotranspiration — Applied to MSG-SEVIRI data in the Senegal River basin. *Remote Sensing of Environment*, *112*, 1242–1255.
Tang, R., Li, Z. -L., & Tang, B. (2010). An application of the Ts–VI triangle method with enhanced edges determination for evapotranspiration estimation from MODIS data in arid and semi-arid regions: Implementation and validation. *Remote Sensing of Environment*, *114*, 540–551.
Venturini, V., Bisht, G., Islam, S., & Jiang, L. (2004). Comparison of evaporative fractions estimated from AVHRR and MODIS sensors over South Florida. *Remote Sensing of Environment*, *93*, 77–86.
Verhoef, W., Jia, L., Qing, X., & Su, Z. (2007). Unified optical–thermal four-stream radiative transfer theory for homogeneous vegetation canopies. *IEEE Transactions on Geoscience and Remote Sensing*, *45*, 1808–1822.
Wan, Z., & Dozier, J. (1996). A generalized split-window algorithm for retrieving land-surface temperature from space. *IEEE Transactions on Geoscience and Remote Sensing*, *34*, 892–905.
Wang, K., Li, Z., & Cribb, M. (2006). Estimation of evaporative fraction from a combination of day and night land surface temperatures and NDVI: A new method to determine the Priestley–Taylor parameter. *Remote Sensing of Environment*, *102*, 293–305.
Yang, J., & Wang, Y. (2011). Estimating evapotranspiration fraction by modeling two–dimensional space of NDVI/albedo and day–night land surface temperature difference: A comparative study. *Advances in Water Resources*, *34*, 512–518.